LABPLAS

Horizon 2020
European Union Funding
for Research & Innovation

# Land-Based Solutions for Plastics in the Sea

*This project has received funding from the European Union's Horizon 2020 research and innovation programme under grant agreement No 101003954*

## D7.8 Multi-parameter settling velocity closure

**Due date of deliverable: 31/05/2023**

**Actual submission date: 31/05/2023**

Horizon 2020
European Union Funding
for Research & Innovation

LABPLAS

Horizon 2020
European Union Funding
for Research & Innovation

## PROJECT INFORMATION

**Project number:** 101003954

**Project acronym:** LABPLAS

**Project full title:** Land-Based Solutions for Plastics in the Sea

**Call:** H2020-SC5-2018-2019-2020 submitted for H2020-SC5-2020-2 / 03 Sep 2020

**Topic:** CE-SC5-30-2020 – Plastics in the environment: understanding the sources, transport, distribution and impacts of plastics pollution

**Type of action:** RIA – Research and Innovation Action

**Starting date:** June 1st, 2021

**Duration:** 48 months

**List of participants:**

| Nº | Participant name | Acronym | Country | Type |
|---|---|---|---|---|
| 1 | UNIVERSIDADE DE VIGO | UVI | SPAIN | HES |
| 2 | UNIVERSIDADE DA CORUÑA | UDC | SPAIN | HES |
| 3 | Bundesanstalt fuer Gewaesserkunde | BfG | GERMANY | RTO |
| 4 | LABORATORIO IBERICO INTERNACIONAL DE NANOTECNOLOGIA | INL | PORTUGAL | RTO |
| 5 | KATHOLIEKE UNIVERSITEIT LEUVEN | KUL | BELGIUM | HES |
| 6 | HELMHOLTZ ZENTRUM FUR OZEANFORSCHUNG KIEL | GEOMAR | GERMANY | RTO |
| 7 | NATIONAL OCEANOGRAPHY CENTRE | NOC | UNITED KINGDOM | RTO |
| 8 | SORBONNE UNIVERSITE | SU | FRANCE | HES |
| 9 | OPEN UNIVERSITEIT NEDERLAND | OUNL | NETHERLANDS | HES |
| 10 | LEIBNIZ INSTITUTE FOR BALTIC SEA RESEARCH | IOW | GERMANY | RTO |
| 11 | ASSOCIACAO PARA O DESENVOLVIMENTO DO ATLANTIC INTERNATIONAL RESEARCH CENTRE | AC | PORTUGAL | RTO |
| 12 | UNIVERSIDADE FEDERAL DO SAO PAULO | UNIFESP | BRAZIL | HES |
| 13 | BASF SE | BASF | GERMANY | LE |
| 14 | TG ENVIRONMENTAL RESEARCH | ER | UNITED KINGDOM | SME |
| 15 | CONTACTICA S.L. | CTA | SPAIN | SME |
| 16 | STICHTING EGI | EGI | NETHERLANDS | Non-P |
| 17 | STICHTING RADBOUD UNIVERSITEIT | RU | NETHERLANDS | HES |
| 18 | UNIVERSIDADE FEDERAL DO PARÁ | UFPA | BRAZIL | HES |

## DELIVERABLE DETAILS

| | |
|---|---|
| **Document number:** | D7.8 |
| **Document title:** | Multi-parameter settling velocity closure |
| **Dissemination level** | PU – Public |
| **Period:** | RP2 |
| **WP:** | WP7 |
| **Task:** | Task 7.6 |
| **Status:** | Final |
| **Author:** | SORBONNE UNIVERSITÉ, KU LEUVEN |
| **Reviewers:** | KU LEUVEN |
| **Recommended citation format** | Pedrotti, M.L., Labis, E., Riom, W., Shettigar, N., Toorman, E.A., 2023, Technical report describing the multi-parameter settling velocity closure - Deliverable 7.8, LABPLAS Grant Agreement No. 101003954 H2020-SC5-2020-2 |
| **Executive summary:** | This report corresponds to deliverable 7.8 which describes the multi-parameter settling velocity closure of the WP7 Modeling, Task 7.6 - Derivation of model parameterizations for MP transport properties. It covers the in situ plastic incubation experiments, experimental analysis of plastic settling velocity, and results. |

| Version | Date | Comments |
|---|---|---|
| 1.0 | 31.Mar.2023 | This is a continuation of deliverable 7.7 where the biofilm growth experiments are presented. |
| 2.0 | 02.Sep.2024 | Extended version to address comments by the PO and reviewer at the RP2 Review Meeting. |

**Disclaimer**

The views and opinions expressed in this document reflect only the authors' views, and not necessarily those of the European Commission.

## TABLE OF CONTENTS

## LIST OF FIGURES

## ABBREVIATIONS AND ACRONYMS

| Abbreviation / Acronym | Description |
|---|---|
| **ADV** | Acoustic Doppler Velocity |
| **CFD** | Computational Fluid Dynamics |
| **DC** | Discrete Classes |
| **DIN** | Deutsches Institut für Normung (German Institute for Standardization) |
| **EDTA** | Ethylene Diamine Tetraacetic Acid |
| **KUL** | KU Leuven |
| **LED** | Light-Emitting Diode |
| **MoM** | Method of Moments |
| **MP** | Micro Plastic |
| **NDF** | Normalized Distribution Function |
| **PBE** | Population Balance Method |
| **PCL** | Poly Capro Lactone |
| **SU** | Sorbonne Université |
| **SW** | Seawater Well |
| **WP** | Work Package |

# 1 INTRODUCTION

Plastic pollution in oceans and rivers has become an environmental threat to ecosystems, aquatic life and human health (Rochman et al 2016, Gall & Thompson, 2015). Global plastic production is growing exponentially, in 2018, plastic production reached 359 million metric tons (Mt) and this quantity is expected to increase tenfold by 2025 (Plastics Europe, 2019), without improvements to the system, an estimated 12 billion Mt of plastic litter will end up in landfills and in the natural environment by 2050 (Geyer et al. 2017).

Although plastic is ubiquitous in the marine environment, knowledge of the transport mechanisms of these particles remains limited and the sources are widespread. Many studies have attempted to quantify plastic leakage into the environment on a global scale. Among them, Jambeck et al. (2015) estimated that 4.8-12.7 Mt of plastic enters the global ocean from land-based sources each year, but the researchers found only a small fraction of the plastic floating to the surface. The discrepancy between plastic inputs and loads, known as the "missing" plastic problem, reflects our lack of knowledge about the key processes that bring and selectively remove plastic debris from the surface. One hypothesis is that ocean currents and sinking are responsible for the removal of plastic waste. Plastic debris can be transported by ocean currents and eventually sink to the ocean floor or be buried in the sediments, making it difficult to detect and measure suggesting that even floating plastic debris eventually loses buoyancy due to biofouling and/or fragmentation and sinks into the sediments (Fazey & Ryan, 2016; Lusher et al., 2015; GESAMP, 2015).

Accurately determining the amount of plastic missing from the ocean remains an open question due to the lack of methods to link plastic losses from the terrestrial system to marine litter, which may result in an over- or underestimation of the amount of plastic litter at the ocean surface. The risk assessment requires knowledge of the transport of particles to the ocean and prediction of where particles are released and where they will be deposited.

Plastic transport is influenced by a range of factors, including environmental constraints, hydrodynamic processes, and dynamic properties, particularly their vertical velocity, whether they are sinking or rising. When modelling the fate and transport of plastic particles, the most critical parameter to consider is their sedimentation rate. Previous studies have demonstrated that plastic transport in water adheres to fundamental principles of fluid mechanics, such as well-established drag laws of an object in relative motion to its ambient medium (Toorman et al., 2002). In addition, the properties of plastic particles can change due to fragmentation, weathering, biofouling, and aggregation, adding additional parameters to consider. Systematic characterizations of the plastic properties are needed to come up with better prediction tools. Biofilm-plastic interactions can alter the buoyancy properties of particles favouring their vertical movement and influencing the fate of microplastics (MP <5mm). Recent work describing settling experiments has been studied in the laboratory using pristine spherical particles with a uniform size distribution (Potthoff et al., 2017) and a few studies describe settling experiments providing new empirical velocity closures (Kowalski et al., 2016; Katmulliana & Isachenko, 2017; Waldschläger & Schutrumph, 2019, Jalón-Rojas 2022, Mendrick et al., 2023).

## Objectives

This deliverable provides experimental data on microplastic (MP) settling rates for the implementation of an Eulerian particle transport model. To this end, we propose to start from the fall velocity closure for spherical particles and then address closure corrections according to the different phenomena to which MP are subject: inertia effect, shape influence, biofouling, hindered settling, turbulence, size distribution, degradation and break up and finally hetero-aggregation. While most of the corrections are approached using literature, biofouling,

and turbulence are discussed with emphasis on the biofouling and settling experiment led at Sorbonne Université (SU) and the turbulence and settling experiment studied at KU Leuven (KUL) in the framework of the PLUXIN project (https://pluxin.be/nl).

This report only addresses particles of size > 2 µm. Below this threshold, the gravity effect (and thus buoyancy) becomes negligible and the particles only follow the motion of the ambient water as a passive tracer.

## 2 Settling of Individual Particles

The particle settling velocity is the primary particle characteristic needed in particle transport or dispersal models. It appears in the particle mass balance equation in the exact form of the actual absolute particle velocity.

Traditionally, the value of the settling velocity is assumed to equal the terminal fall velocity of the particle. However, the latter is obtained from measurements in quiescent water.

The fall velocity can be approximated from the following hierarchical corrections, starting from the exact theoretical fall velocity for spherical particles at low speed (i.e. in Stokes or creeping flow regime):

1) Inertial correction
2) Shape correction
3) Biofilm correction ➔ change in size and density
4) Hindered settling correction
5) Size distribution correction
6) Degradation break-up correction ➔ change in size distribution
7) Hetero-aggregation correction ➔ change in size and density

**Colloidal regime:** When the particle is very small in size, typically < 2 µm, *independent of the particle density*, the particle motion becomes dominated by the temperature-induced Brownian motion of the water molecules. Gravity has a negligible effect on such small particles. They do not settle (or rise), but follow the motion of the ambient water as a passive tracer.

**Gravitational regime**: For particles with sizes above 2 µm, the effect of gravity starts to become increasingly important with increasing size. The settling/rising behaviour is then characterized by the "fall/rise velocity". The fall/rise velocity is the *terminal* settling/rising velocity in *quiescent* water when the buoyant weight is outbalanced by the counteracting drag force from the displaced water (Hoerner, 1965), mathematically expressed by the force balance equation:

$$\rho_w C_D A_p \frac{{w_p}^2}{2} = g(\rho_p - \rho_w)V_p \qquad (1.)$$

where: $w_p$ = the particle velocity, $g$ = the gravity constant (9.81 m/s$^2$), $\rho_p$ = the particle density, $\rho_w$ = the water density, $A_p$= vertically projected cross-sectional area of the particle, $V_p$= particle volume, $C_D$ = the drag coefficient. This equation can be solved for the fall velocity:

$$w_p = \sqrt{2\frac{g}{C_D}\left(\frac{\rho_p}{\rho_w} - 1\right)\frac{V_p}{A_p}} \qquad (2.)$$

Particles with a density larger than that of water will sink; those with lower density will rise. A closure for the drag coefficient is required to compute $w_p$.

## 2.1 Stokes fall velocity

The only exact value of the fall velocity can be computed for a perfectly smooth spherical particle in very slow relative motion (called "creeping flow"). It can be demonstrated that the drag coefficient for a sphere in creeping flow follows the relationship:

$$C_{D0} = \frac{24}{\mathrm{Re_p}} \tag{3.}$$

with $\mathrm{Re}_p = \frac{w_p d_p}{\nu}$ = the particle Reynolds number, $d_p$ = the particle size, $\upsilon$ = the kinematic viscosity of the ambient fluid.

Inserted into equation (2), the so-called Stokes (1851) fall velocity $w_0$, is obtained as:

$$w_0 = \frac{(\rho_p - \rho_w) g d_p^2}{18 \mu_w} \tag{4.}$$

where: $d_p$ = the particle size, $\mu_w (= \rho_w \nu)$ = the dynamic viscosity of water. This formula is valid for very slow flow conditions, i.e. *creeping* flow, where the particle Reynolds number $\mathrm{Re}_p = \frac{w_p d_p}{\nu} << 1$.

The viscosity of water varies significantly with temperature and salinity and can have a significant effect on the value of the fall velocity, certainly for plastic polymers with density close to that of water. Notice that the proportionality with the density difference implies that the "settling" velocity closure also applies to *rising* particles with densities smaller than water, resulting in a negative (i.e. upward-directed) fall velocity.

## 2.2 Inertia correction

For many micro- (and macro-) particles the particle Reynolds number is usually larger than 1. In that case, the flow around the particle does not stay laminar, but a boundary layer develops which becomes unstable and turbulent. In the downward side of the particle, the boundary layer tends to detach, forming a wake. In this wake the pressure drops, resulting in a larger fall resistance, causing an increase in the drag force, and subsequently a slower settling than predicted by Stokes law. To take that effect into account, an empirical correction is applied, as it cannot be determined theoretically. Two major methods exist.

In the first method, the drag (i.e. resistance) coefficient is corrected with an empirical function of the particle Reynolds number. Throughout the history of fluid mechanics, many different formulae have been proposed, and have been reviewed in many subsequent publications.

A popular drag coefficient closure in sediment transport is the one proposed by Schiller & Naumann (1933) but is valid only for $\mathrm{Re_p} < 800$. To extend the validity of this form to higher Reynolds numbers, Clift & Gauvin (1970, 1971) extended the formulation with an extra term, extending the range of validity up to $\mathrm{Re_p} < 10^5$:

$$C_D = C_D\left(1 + a_1 \mathrm{Re}_p^{\,n_1}\right) + \frac{a_2}{1 + a_3 \mathrm{Re}_p^{\,-n_2}} \tag{5.}$$

The five coefficients have subsequently been improved by additional validation data and more accurate data fitting techniques (Table 1).

**Table 1**

| Authors | $a_1$ | $n_1$ | $a_2$ | $a_3$ | $n_2$ |
|---|---|---|---|---|---|
| Schiller & Naumann (1933) | 0.150 | 0.687 | 0 | - | - |
| Clift & Gauvin (1970) | 0.150 | 0.687 | 0.42 | 42500 | 1.16 |
| Turton & Levenspiel (1986) | 0.173 | 0.657 | 0.413 | 16300 | 1.09 |
| Haider & Levenspiel (1989) | 0.1806 | 0.6459 | 0.4251 | 6880.95 | 1 |

A major disadvantage of this form is the fact that the drag coefficient correction requires the knowledge of the yet unknown fall velocity. Therefore, one has to apply an iteration, typically starting from the Stokes formula.

In the second method, settling velocity and particle size are non-dimensionalised differently, i.e. using the particle-independent parameters fluid (kinematic) viscosity ($\upsilon$) and the gravity constant ($g$):

$$\boldsymbol{w_* = \frac{w_p}{(g'\upsilon)^{1/3}}} \qquad \textbf{(6.)}$$

and

$$\boldsymbol{d_* = d\frac{(g'\nu)^{1/3}}{\upsilon} = d\left(\frac{g'}{\upsilon^2}\right)^{1/3}} \qquad \textbf{(7.)}$$

where: $g' = (\gamma - 1)g$ and $\gamma = \rho_p/\rho_f$ = the specific particle density.

$d_*$ is actually nothing else than the 3rd root of the Archimedes number ($\mathrm{Ar}$), the ratio of gravitational forces to viscous forces[1] (also called the Galileo number, $\mathrm{Ga}$)[2]. The use of this scaling to particle settling has become known through the work of Hallermeier (1981) and Dietrich (1982), who applied a complex empirical fitting to experimental data for spheres and sand grains.

Turton & Clark (1987) proposed a much simpler formula by applying power blending of the asymptotic behavior from the Stokes solution to a constant value at very high Reynolds numbers:

$$\boldsymbol{w_* = \left(\left(\frac{{d_*}^2}{18}\right)^{-n} + \left(\frac{\sqrt{d_*}}{\alpha}\right)^{-n}\right)^{-1/n}} \qquad \textbf{(8.)}$$

where $\frac{{d_*}^2}{18}$ is the equivalent non-dimensional Stokes solution. Different values have been proposed by various authors (table 2).

**Table 2**

| Authors | $\alpha$ | $n$ |
|---|---|---|
| Turton & Clark (1987) | 0.321 | 0.824 |
| Toorman (2022) | 0.52 | 0.75 |

[1] https://en.wikipedia.org/wiki/Archimedes_number

[2] Note that Fornari et al. (2016) define $\mathrm{Ga} = \sqrt{\mathrm{Ar}}$.

The original particle Reynolds number and drag coefficient are easily retrieved as:

$$\mathbf{Re}_p = w_* d_*$$
$$C_D = \frac{4}{3}\frac{d_*}{{w_*}^2} \quad \textbf{(9.)}$$

Camenen (2007) demonstrates that this leads to the general form:

$$\frac{w_p d_p}{\nu} = \mathbf{Re}_p = \left(\sqrt{\frac{1}{4}\left(\frac{A}{B}\right)^{2/m} + \left(\frac{4{d_*}^3}{3B}\right)^{1/m}} - \frac{1}{2}\left(\frac{A}{B}\right)^{1/m}\right)^{1.5} \quad \textbf{(10.)}$$

With values of the parameters, depending on the data set used for calibration (table 3).

**Table 3**

| Authors | Material | $A$ | $B$ | $m$ |
|---|---|---|---|---|
| Dallavalle (1948) | Spheres | 24.0 | 0.40 | 2 |
| Julien (1995) | natural sand | 24.0 | 1.50 | 1 |
| Sousby (1997) | natural sand | 26.4 | 1.27 | 1 |
| Cheng (1997) | natural sand | 32.0 | 1.00 | 1.5 |

Several formulas of the form of eq.(10) can be found in the literature (Kaskas, 1964; Cheng, 1997; a.o.). However, we propose to stick to the very simple form of equation (8).

## 2.3 Shape correction

As a significant part of MP litter comes from abrasion, erosion, and fragmentation of bigger-sized plastics, their shape is never perfectly spherical. As soon as the shape of the particle deviates from a perfect sphere, the drag changes (e.g. Hoerner, 1965; Janke, 1966). Several studies comprise experimental data for the drag of non-spherical particles as a function of the Reynolds number. These data show that the high-Reynolds asymptotic value is usually higher than for a spherical particle (Figure 1).

The deviation from a perfect spherical parameter introduces a problem in the characterisation of the particle by a single characteristic size. In the literature, the definition of this equivalent particle size is not always clearly stated. Most authors use the equivalent spherical diameter, the diameter of a sphere having the same volume as the particle (e.g. Haider & Levenspiel, 1989). Different proposals are found in the literature to introduce additional parameters to characterize the deviating drag as a result of a non-spherical shape.

Wadell (1932) introduced the (operational) particle sphericity ($\psi$) as the ratio of the volume of the particle to that of the smallest circumscribing sphere. Following Krumbein (1941), this can then be *approximated*, using the three principal axes of a particle:

$$\psi = \frac{d_a d_b d_c}{{d_a}^3} \quad \textbf{(11.)}$$

where $d_a$ = the largest size, $d_b$= the intermediate largest size, measured perpendicular to the $a$-axis, and $d_c$ = the smallest size, measured perpendicular to both the $a$- and $b$-axis.

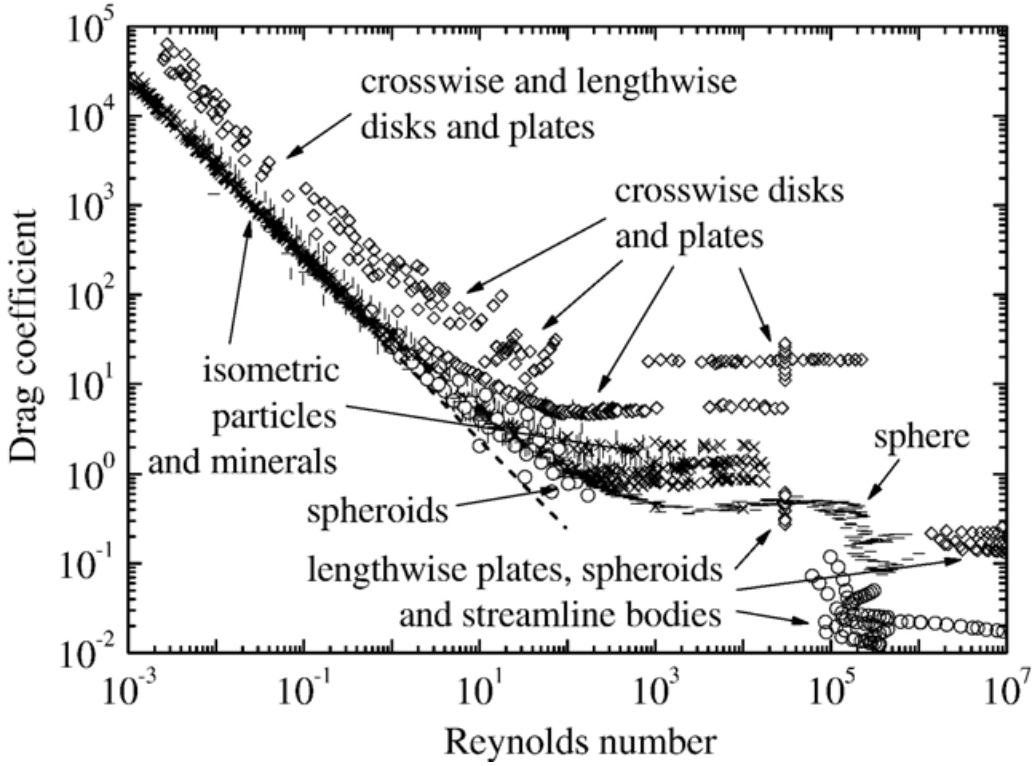


**Figure 1**. Drag coefficient of differently shaped particles from the literature as a function of the Reynolds number. ----, Stokes; - , spheres; ◊, disks and plates; ×, isometric bodies; |, minerals; ◯, spheroids and streamlined bodies, collected by Hölzer & Sommerfeld (2008).

This equation actually is the ratio of the volume of an ellipsoid to that of its circumscribing sphere. Haider & Levenspiel (1989) define another sphericity ($\phi$) as the ratio of the surface of a sphere having the same volume as the particle and the actual surface area of the particle.

A popular alternative is the Corey (1949) shape factor, defined as:

$$C_{sf} = \sqrt{\frac{{d_c}^3}{d_a d_b d_c}} = \frac{d_c}{\sqrt{d_a d_b}} \qquad \textbf{(12.)}$$

This equation actually is the square root of the inverse ratio of the volume of an ellipsoid to that of its largest inscribing sphere.

Also, the surface angularity and roughness, characterized by the roundness parameter (Briggs et al., 1962), affect the drag force (Williams, 1966).

Table 4 gives an estimation of these parameters for different kinds of particles.

Several proposals are found in the literature on how to adapt fall velocity closure equations for spherical particles to particles of other shapes (e.g. Dietrich, 1982; Leith, 1987; Camenen, 2007; Hölzer & Sommerfeld, 2008); Digouardi & Mele, 2015; Digouardi et al.,2018).

**Table 4.** Shape factors for specific particles from Camenen (2007) and Haider & Levenspiel (1989).

| Material | $C_{sf}$ [0 -1 ] | $P$ [0-6] | $\phi$ [0-1] |
|---|---|---|---|
| Spherical particles | 1 | 6 | 1 |
| Smooth cobbles | 0.7 | 5 | |
| Natural sand | 0.7 | 3.5 | |
| Crushed sand | 0.7 | 2 | |
| Long cylinders | 0.4 | 5 | |
| Silt, cohesive particle | 0.4 | 2 | |
| Flocs | 0.6 | 1 | |
| Octahedrons | | | 0.85 |
| Cubes | | | 0.8 |
| Tetrahedrons | | | 0.67 |

Interestingly, also the simple power-blending equation of Turton-Clark (1987), eq.(8), has been extended to application to non-spherical particles by Haider & Levenspiel (1989), which resulted in the following closure for the model parameters, valid for isometric particles ($\phi > 0.5$):

$$\boldsymbol{\alpha = \frac{3}{4}(3.1131 - 2.3252\phi)} \text{ and } \boldsymbol{n = 1} \qquad \textbf{(13.)}$$

The model was calibrated with several data sets, shown in Figure 2.

However, the disk data (dashed lines) was fitted with the Clift & Gauvin formula (eq.5) with much more complex model parameter closures.

Toorman *et al.* (2018) analysed many data sets for differently shaped plastic particles available at the time. In particular, for the data from Khatmullina & Isachenko (2016) on cylindrical PCL particles of different diameters and lengths, they noticed that the traditional choice of an equivalent diameter for both the drag coefficient and the particle Reynolds number did not allow to generate $C_D - Re$ graphs of the usual shape. The most meaningful graph was obtained by taking the cylinder length as the length scale for the Reynolds number and the diameter for the drag coefficient. The asymptotic $C_D$ value then not unexpectedly was comparable to the well-document value for cylinders.

More researchers have concluded that a fall velocity closure for non-spherical particles requires not one, but two shape parameters.

Camenen (2007) uses the Corey shape factor and the roundness (P - estimated using the scale of Briggs et al., 1962) to define empirical relations to express the coefficients $A$ and $B$ of eq.(10) in terms of these parameters.

Hölzer & Sommerfeld (2008) propose a formula, starting from the earlier work of Leith (1987). Leith uses as representative size the diameter of a sphere with the same volume as the object ($d_V$).

$$C_D = \frac{8}{Re}\frac{1}{\sqrt{\phi_\perp}} + \frac{16}{Re}\frac{1}{\sqrt{\phi}} + + \frac{3}{\sqrt{Re}}\frac{1}{\phi^{3/4}} + \frac{0.4210^{0.4(-\log\phi)^{0.2}}}{\phi_\perp} \quad \textbf{(14.)}$$

where: $\phi$ = the sphericity and $\phi_\perp$ = the crosswise sphericity.

Digouardi *et al.* (2018) use a shape factor defined by Dellino *et al.* (2005) $\Psi = \Phi/X$, i.e. the ratio between sphericity $\Phi$ and circularity $X$.

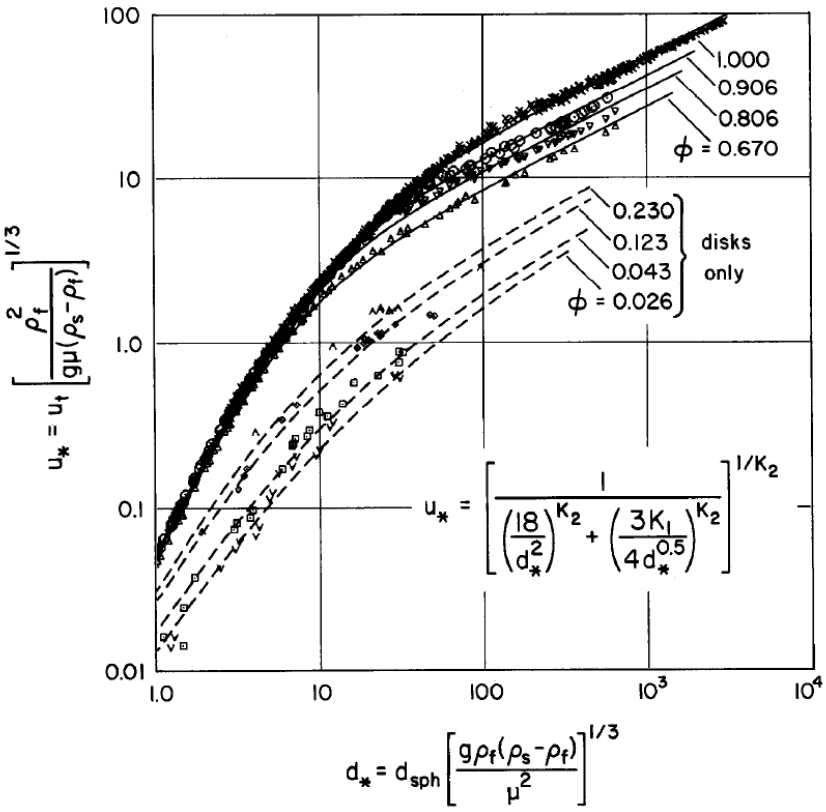


**Figure 2**. Validation of the power-blending closure, eq.(8), adapted for isoparametric particles (full lines) and another fitting relation for disks based on eq.5 (dashed lines) by Haider & Levenspiel (1989)

Kramer *et al.* (2021) have collected the largest set of particle settling velocities (for a wide variety of particles) from the literature and added additional data from new experiments they carried out. Figure 3 presents these data in the traditional form of drag coefficient as a function of particle Reynolds number, with a colour scheme depicting the Corey shape factor. One can deduce the following lessons from this graph:

- For (Corey) shape factors > 0.3, i.e. "granular" particles, the effect of shape factor starts for Re > 0.1 and the deviation from a spherical particle increases with Re up to one order of magnitude (a factor 10) at Re = 10,000.
- This uncertainty of a factor 10 is also the range for an experiment with the same individual particle that is repeated multiple times, cf. the experiments carried out during the JPI Oceans WEATHER-MIC project (Toorman *et al.*, 2017; Toorman *et al.*, 2018) and the additional experiments by Kramer *et al.* (2021). This uncertainty is explained by the fact a non-spherical particle is also rotating during its settling,

during which the projected area perpendicular to the vertical direction alternates, resulting in an unpredictable irregular fluctuating motion due to varying vortex shedding. The result is highly sensitive to the initial conditions (i.e. the position and release of the particle).

- Few reliable data are found for shape factors < 0.3. Particles with a shape factor in the range of 0.3-0.1 can be called "flat", while particles with a shape factor < 0.1 tend to become 'needle' or 'fibre' shaped. These particles typically lie above the data for granular particles. Repeated experiments with these particles indicate that the uncertainty for flat particles is two orders of magnitude and for fibres even 3 orders of magnitude. This is easily explained for flexible material particles, like foils and fibres which can change their shape during their motion (Bagaev *et al.*, 2017).

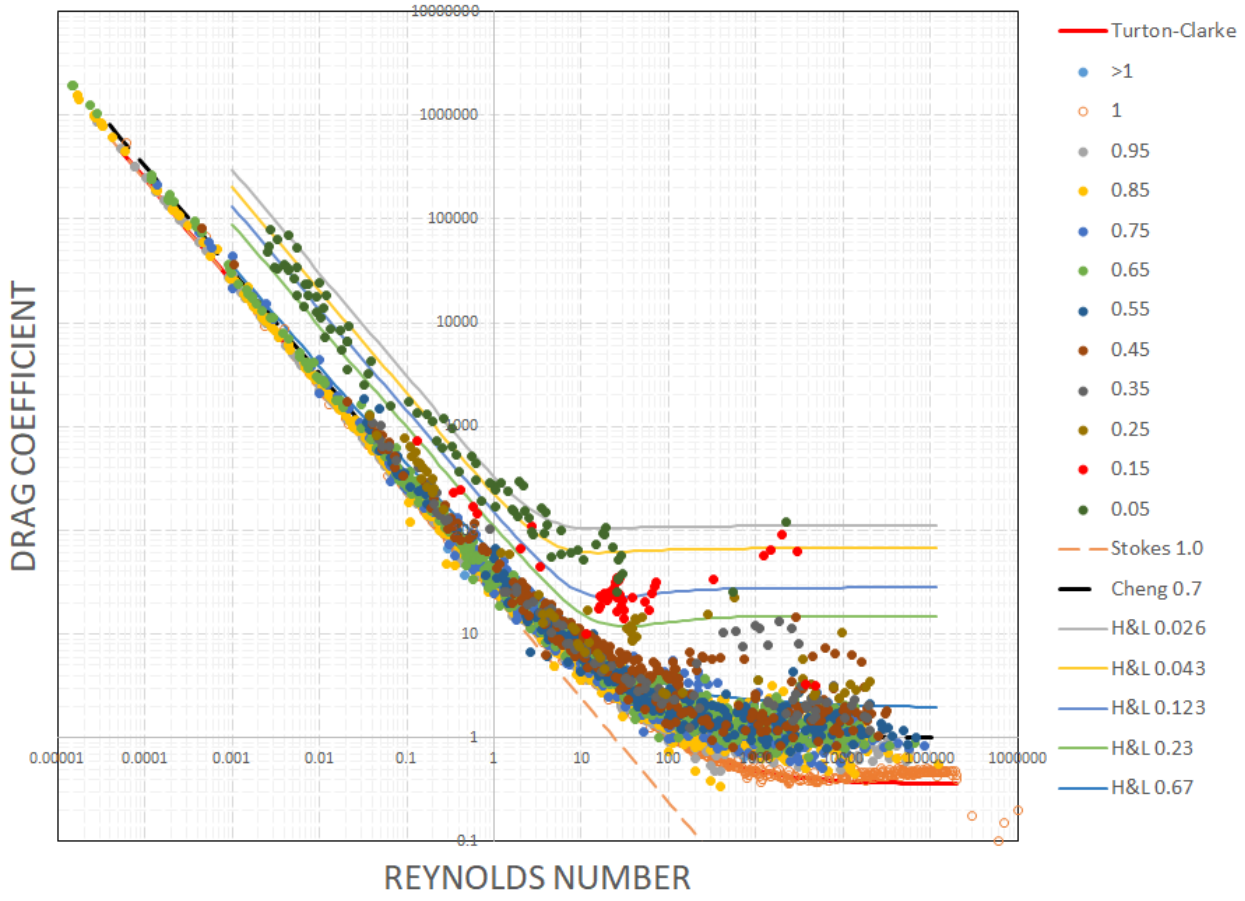


**Figure 3**. Data (dots) collected by Kramer et al. (2021) grouped by spericity compared with the Stokes (1852) theoretical closure and empirical relations by Turton & Clarke (1987), Cheng (1997) and Haider & Levenspiel (H&L) (1989) for various Corey shape factor values.

In addition:

- The motion of colloidal particles (size < 2 µm) is dominated by Brownian motion and should be modelled as passive tracers.
- The motion of flat particles (and coiled fibres) is very much determined by the motion of the fluid as they are also prone to lift and drag by flow in the horizontal direction, increasing the likeliness to rotate

the particle (cf. autumn leaves or a parachute in a string wind). It could explain why plastic bags can be found in suspension at any depth in the water column of flowing streams.

- The smaller the shape factor, the more problematic the choice of length scale for the calculation of the Reynolds number becomes. For cylindrical particles, it was found in the WEATHER-MIC project that choosing the cylinder length resulted in a much more "normal" $C_D - \mathrm{Re}$ relation, which could be explained that by the fact for increasing length, the drag is dominated by the form drag of the circular cross-section (Toorman *et al.*, 2018).

### 2.4 Recommendations for future research

The total drag is actually the sum of two contributions, i.e. skin friction and form drag. For the Stokes formula, for instance, it is known that skin friction accounts for 2/3 of the total drag (Leith, 1987). The skin friction must be proportional to the total particle surface, while the form drag depends on the projected particle area perpendicular to the motion and the shape. The latter is expected to be determined by the largest two primary sizes: $A_\perp = \frac{\pi}{4} d_a d_b$

Possibly the skin friction area could be approximated with the thickness (= smallest size $d_c$) of the particle and the perimeter of the perpendicular drag surface ($P = \pi\sqrt{d_a d_b}$) $\rightarrow A_{sf} = P d_c = \pi\sqrt{d_a d_b} d_c$

Therefore, since skin friction and form drag are governed by different particle areas, it would actually make more sense to split the total drag force into two distinct contributions to develop a more versatile fall velocity closure for non-spherical particles.

This is work for future more fundamental research, which is expected to receive help from particle resolving computational fluid dynamics, which is still in full development, due to its complexity.

The simplification of the large variability of MP in shape and sizes (pellets, films, fragments, fibers, foams) to just one or two parameters including a set of equations is naturally far from exact. Additionally, the exhaustive knowledge of all individual MP litter characteristics (the three principal axes, angularity, roundness, density, …) is not achievable. Hence the experimental validation of these closures is often not straightforward and includes a lot of deviation.

Therefore, in the absence of an accurate closure, *for the time being*, we propose to use an equation of the form of equation (8) with parameter values calibrated for the average shape factor 0.7. The resulting equation is presented in the Conclusions (section 8).

## 3 BIOFOULING

The formation of biofilm associated with plastic was studied as well as their sedimentation rate at different time scales. Recent work describing settling experiments has been studied in the laboratory using pristine spherical particles with a uniform size distribution (Potthoff et al. 2017) and a few studies describe settling experiments providing new empirical velocity closures (Kowalski *et al.*, 2016; Katmulliana & Isachenko, 2017; Waldschläger & Schutrumph, 2019; Jalón-Rojas, 2022; Mendrick *et al*., 2023).

## 3.1 Material and methods

In our experiment, the colonization of MP was followed by incubating already weathered particles *in situ,* and the sedimentation rate was studied in the laboratory in a sediment column. The plastics were collected with a manta net at the surface (floating plastics) and previously cleaned, these "aged plastics" are left in incubation at sea, recovered, and tested in the laboratory in the sedimentation column until they settle. This mimics a stranding-resuspension event of plastics being washed ashore and resuspended to be re-colonized. This technique is more realistic than the use of virgin plastic or the artificial aging of plastics which is often long and difficult to develop.

### 3.1.1 Plastic collection and in situ incubations

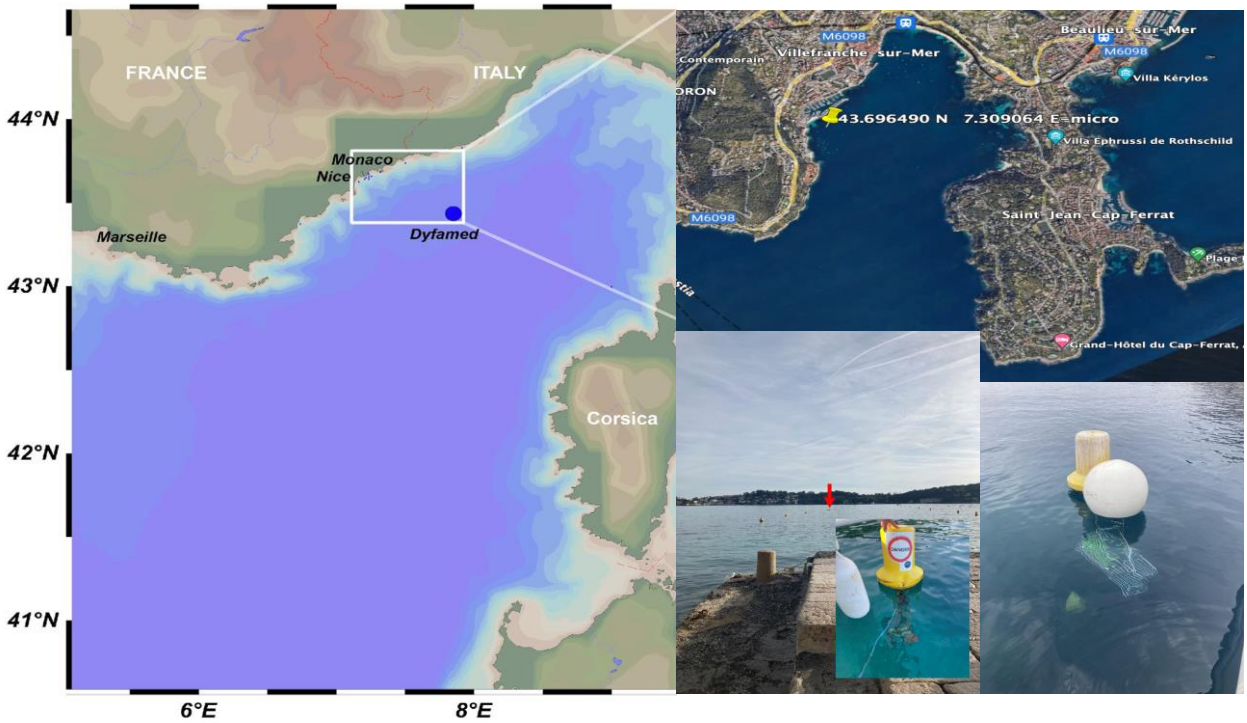


**Figure 4.** Collection of plastics in the surface waters of the north-western Mediterranean Sea between Nice and Villefranche sur Mer and location of the site where the plastics were incubated inside the harbour and a submersed cage used to incubate plastics.

The experiment started in October 2022. Floating plastics were collected with a Manta net (300 µm) in the coastal surface areas of the Villefranche-sur-Mer Bay. Once arrived at the laboratory plastic was cleaned and placed for 48h in an oven at 50°C to remove all biological material. Plastics with a size of 5 mm or more were recovered and larger ones were cut into pieces of 5 to 10 mm and incubated in cages inside the bay (43.696490 N; 7.309064 E) to increase the biofilm formation. The plates are gathered and secured together with cable ties and fixed in a rigid iron cage. A Hobo temperature sensor has been programmed to measure and store the temperature every hour and is also fixed in the cage. The cage is attached to a buoy 50 cm below the surface, located 100 meters from the coast.

Plastics were then placed individually in wells of perforated plates containing 24 wells each to let the surrounding water circulate around the plastics. Each plastic is identified by the location it occupies in the well of the plate and was kept throughout the experiment to track its progress. During placement and further experiments, the plastics are kept in contact with filtered seawater added to the wells.

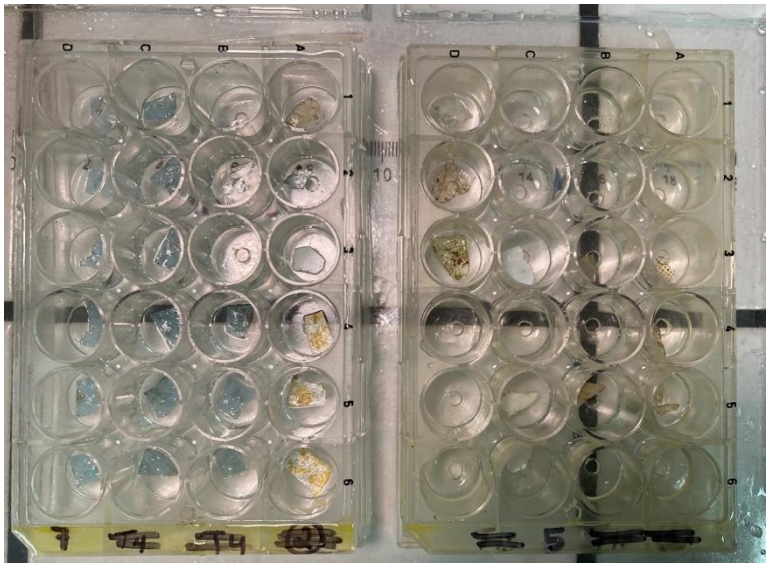

**Figure 5**. Example of two plates incubated in the sea.

### 3.1.2 Characterization of plastics

Seven experiments were conducted at 28, 43, 65, 90, 105, 123, and 153 days after initial incubation, respectively. Several parameters were recorded at the beginning, during each experiment from the rate of rise to the settling of the plastic, and once the plastic had settled.

#### 3.1.2.1 Plastic wet and dry mass and biofilm biomass

The dry mass of the plastics was measured 3 times with a precision balance at the beginning and end of the experiment once the plastic had settled. The wet mass of the plastic was measured at the beginning of the experiment and during each rate-of-rise experiment until the plastic settled, and once the plastic had settled. For that, the plastic was removed from the seawater well (SW), and placed on an aluminium foil in the tared balance, after the first measurement the plastic is returned to its well, and the operation is repeated 3 times. The biofilm biomass was measured in the end once the plastic had settled by weighing plastics with biofouling and after detaching organisms. For that plastic with biofilm was individually replaced in the wells at ambient temperature and the wells were filled with a homogenization buffer composed of Tris HCl 400 mM, EDTA 60 mM (372,23 g/mol), NaCl 105 mM (58,44 g/mol), SDS 1% during at least 3 hr. The homogenization buffer contains chelator ions able to detach the flora and biofilm present. The buffer was removed by aspiration with the aid of a vacuum pump then each well was rinsed with distilled water several times. Plastics were then soaked in a solution of 2.5-to x% Sodium hypochlorite solution (NaClO) for 3 hours at ambient temperature. The solution was then removed in each well by aspiration and plastic was thoroughly rinsed with distilled water as many times as necessary for the complete elimination of the attached flora. After detaching the organisms attached plastic dry mass was again measured and the difference between the two measurements gave the biofilm biomass.

#### 3.1.2.2 Thickness, Size, Biofilm Coverage

The thickness of each plastic was measured 3 times with the Mitutoya micrometer. The size of the plastics was measured from the calibrated images of the plastics. Plastics were individually imaged using a Zeiss Discovery V12 stereomicroscope at magnifications of 10-100x coupled to an imaging system and the ZEN software. To assess biofilm coverage zenith images were taken using Images that were then analysed using ImageJ software, a binary transformation of the image was performed creating a mask, with a chosen threshold range that includes all pixels that are covered by the attached organisms. Plastic was categorized into 6 types: Fragment, Fibre, Film, Filament, Pellets, and foam. The colour of the plastics is defined according to the following criteria: White, Transparent et Translucent, Blue, Green, Yellow/Golden, Red/Pink, Brown, Black, and Grey.

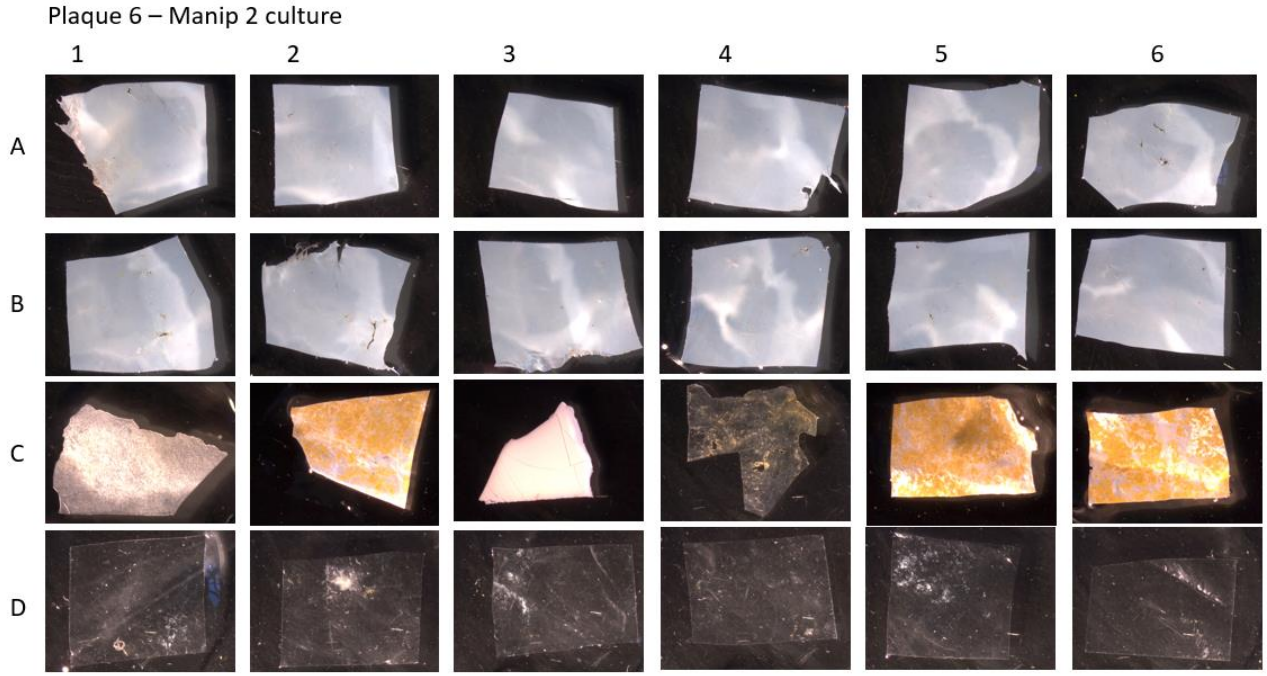


**Figure 6**. Reconstruction of the composition of a plastic plate photographed before the experiment.

#### 3.1.2.3 Density determinations

Particle density was estimated using a variation of the titration method according to DIN 53479 (ISO, P., 2019). and previous experimental studies (Jalón-Rojas *et al.*, 2022).

**Initial density by titration (Ethanol-Water miliQ) - Batch Titration of Plastics without Biofilm (*Optimizing Handling Time and Ethanol Usage*)**

The polymers' chemical composition of the plastics used in this experiment was not known at the start of the experiment. To determine their density (kg/m³), a titration method was employed. Since the plastics were collected floating in seawater, which typically has a density of about 1,025 kg/m³ due to the presence of salts and other dissolved substances, we used MilliQ water (density = 999.973 kg/m³) and ethanol (density = 789.979 kg/m³) as the testing mediums. For plastics derived from the same fragment, density was estimated only once. A dilution range of pure ethanol in distilled water was prepared to classify the plastics into titration batches. 100 ml of the solution was placed in a 150 ml glass beaker. This step was repeated at the conclusion of the experiment once the biofilm was removed. All plastics were first transferred into pure MilliQ water to confirm

they were floating, indicating a density below 999.973 kg/m³. Subsequently, the plastics were transferred into pure ethanol to ensure they all sank, confirming a density above 789.979 kg/m³. Each batch of plastics was then titrated with distilled water. After each addition of water and thorough mixing by shaking, the temperature was measured. It was essential that the temperature did not fluctuate by more than 1°C; if it did, the mixture was allowed to stabilize for a few minutes. To minimize temperature variations, the beaker containing the plastics to be titrated was kept in a water bath at room temperature. Water was added incrementally, milliliter by milliliter, until the particles reached neutral buoyancy, where they remained suspended in the liquid for at least 1 minute without rising or sinking (Khatmullina & Isachenko, 2017).

At this point, 10 ml of the mixture was extracted in two steps using a 5 ml pro pipette and transferred to a pre-weighed 15 ml tube. The titrated plastic was then removed from the beaker. This procedure was repeated for each plastic in each ethanol solution batch, with the mass of each tube measured three times.

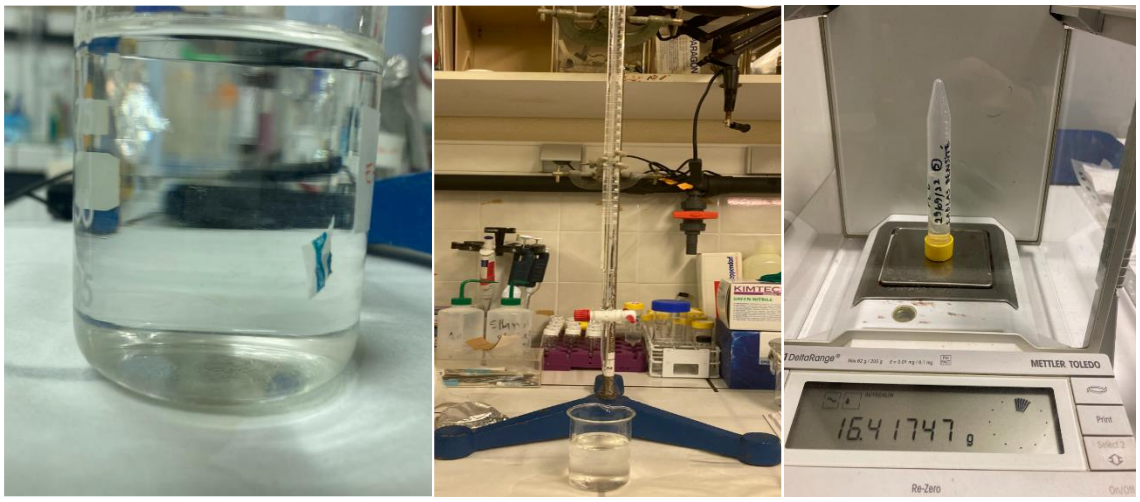


**Figure 7.** The titration experiment

The density of the plastic was calculated as follows:

- Density (kg/m³): The mass of the titrated solution was measured with a scale and then divided by its volume (10 ml) to obtain the solution's density, corresponding to the density of the suspended plastic.
- Specific Density (dimensionless): The calculated density was then divided by the density of distilled water to obtain the specific density of the suspended plastic.

#### 3.1.2.4 Plastic rising and sinking velocity

The experimental setup was adapted from Waldschläger & Schüttrumpf (2019) to measure both, the ascent and descent speeds of plastics. It consists of a transparent column made of plexiglass. The column is 1m high and 20cm in diameter and is large enough to neglect any wall effects (Baba & Komar, 1981). To support the column, a metallic structure was constructed, and a valve was installed at the base of the column to allow the injection of plastics from below. Lighting is provided by an LED bar attached to one of the column support posts. The temperature in the room is set so that the water in the column is around 20°C, and the column is filled with seawater collected from the Bay of Villefranche sur Mer just before the experiment. The plastic is then subjected to the same conditions as the ones in which it will be incubated. Overall, the experimental setup seems well-designed to measure the ascent and descent speeds of plastics under controlled conditions.

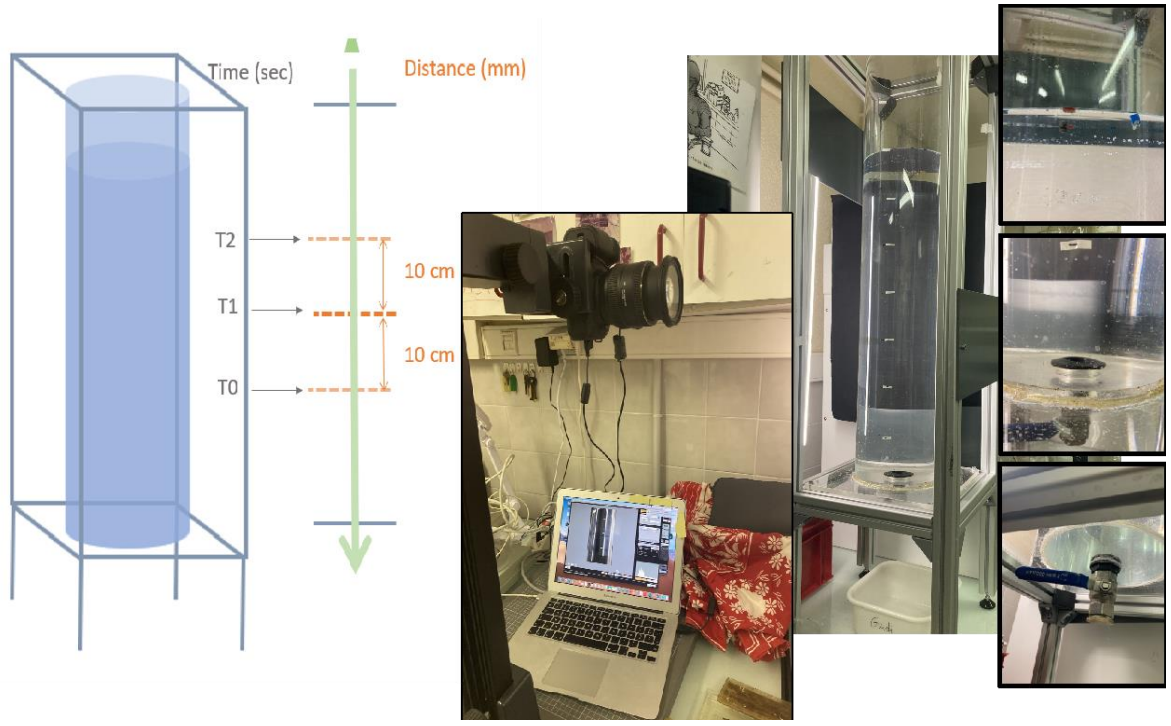


**Figure 8.** Images of the experimental device. For rising experiments, the microplastics are introduced at the base of the column through a valve which, once closed, allows the particle to rise all along the column to be finally recovered at the free surface.

The experiments were conducted every 3 weeks to 1 month, during which the rate of rise or fall of plastics was recorded. For the rising experiments, the plastic was placed in a cap that was screwed under the column, and the valve was opened to inject the plastic from the bottom of the column. The plastic then rose to the surface and was recovered, with a triplicate ascension into the column performed for each particle. For the experiments that studied sedimentation rate, the plastics were placed at the top and centre of the column at a depth of about 1 cm to avoid surface tension. The migration of plastic was recorded using a Canon EOS 6D Mark II Camera. The rise and fall velocities of individual particles were calculated by measuring the time it takes for a particle to move along a baseline of known distance, which was set at 20 cm and positioned 15 cm from the top and bottom of the water column to allow the particle to reach terminal velocity. To preserve the biofilm living on their surface, the plastics for the experiments were kept in a tray of seawater. After the three passes, the plastic was returned to its original well and plate, and either put back into the sea. Overall, the experimental setup seems to have been carefully designed to measure the rate of rise or fall of plastics in a controlled environment, while minimizing the potential impact on the biofilm living on the plastic surface. Three other polystyrene polymer sphere particles (Cospheric LLC, https://www.cospheric.com) were used to validate the experiments, with a certified average diameter of 4.9 mm (±0.1 mm) and 1.94 mm (±0.05 mm) with a certified density of 1.03 g/cm$^3$ and a certified average diameter PS sphere of 4.95+/-0.05mm with a certified density of 0.9 4.9 g/cm$^3$.

***Velocity calculation:*** The velocity of the plastics is then determined by noting the time it takes a plastic to travel the distance between the 20 cm markers attached to the column. The 3 velocity replicates are measured for each plastic.

## 3.2 Results

The average temperature between experiments was in average 19°C. In total, 7 plates were incubated with 159 plastics, 18 are still submerged because they have not sunk yet. This corresponds to the plastic fragment because 100% of the plastic films have sunk. 61 plastics were lost in the field during the last storm in February 2023 or in the laboratory before the end of the experiment. 80 particles sank and their density was measured. The average thickness of the plastic is 0.244 mm (SD 0.38) ranging from 0.01867 to 1.88300 mm. The size of the plastics varies from 4.5mm to 12mm. The typology of plastics used in the experiment was composed of films, the most common forms, 73.09% followed by fragments (26.31%) and foams (0.58%), there are no filaments. The colour of plastic is mainly transparent, white blue and red respectively (35%, 34%, and 24%,5%).

### 3.2.1 Biofilm coverage and wet mass

The assessment of the coverage of the different plastic types over time increases with incubation time, with the percentage coverage changing accordingly. The wet mass increased on average from 0.020 to 0.060g (Figure 9) and the biofilm-colonized surface area increased by an average of 34% relative to the total plastic surface area after 28 days of incubation. At the time of particle flow, the average biofilm coverage was 60% (Figure 10). It is important to note that when analysing these data, the size of the individual particles and their dry weight must be considered.

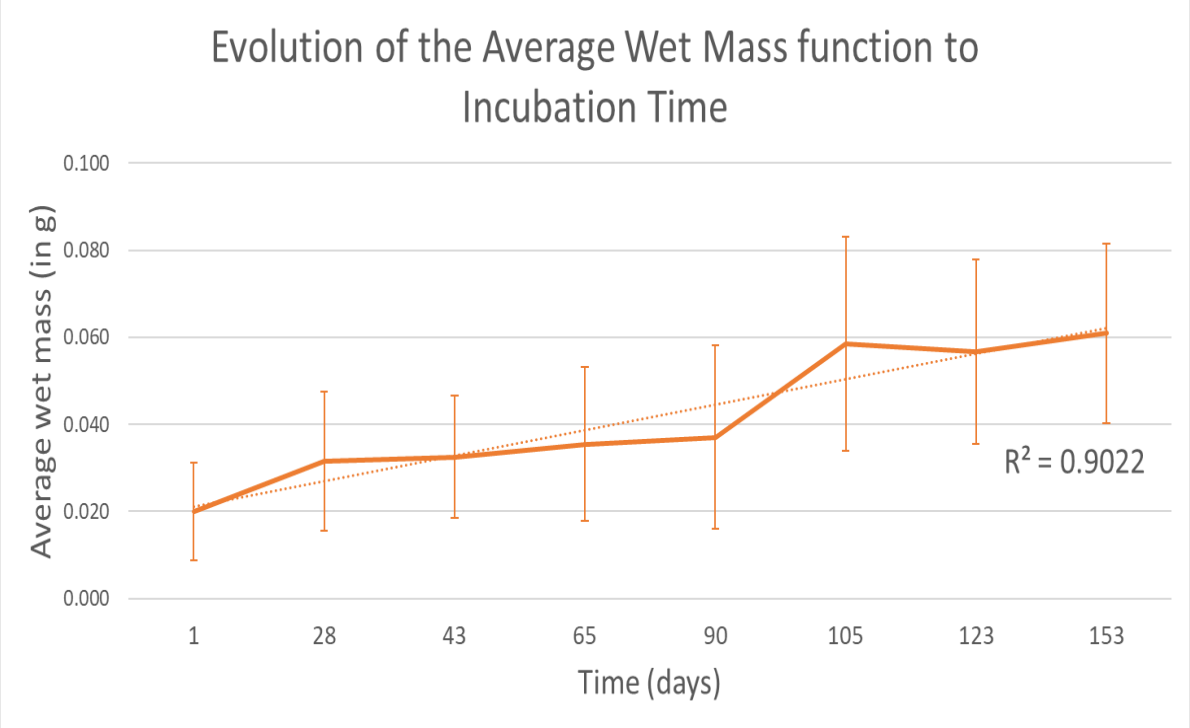


**Figure 9.** Evolution of the average biofilm coverage (%) in two incubation conditions. Blue: at sea; green: in culture with a linear trend line.

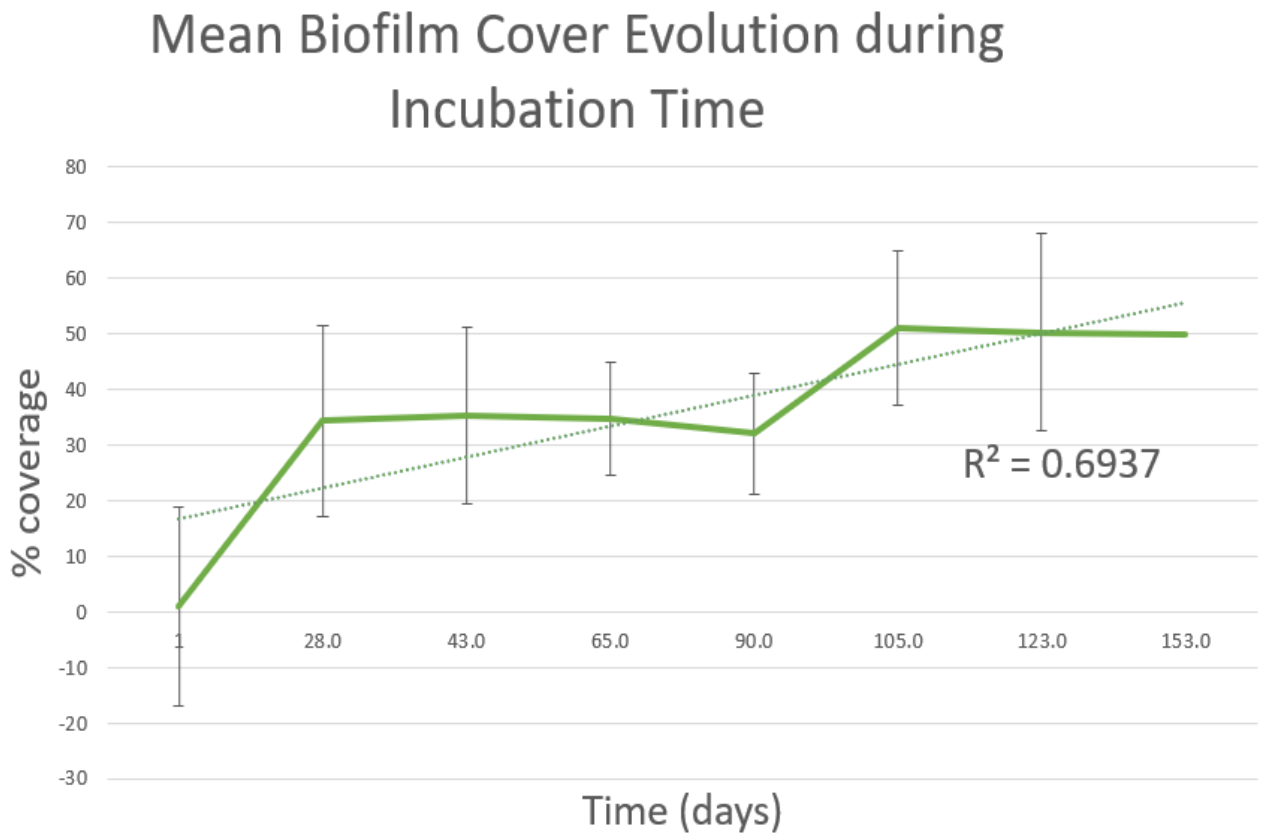


**Figure 10.** Evolution of the average wet mass (g) with linear trend line.

### 3.2.2 Dry and wet mass of plastic and biofilm biomass

The dry mass of the plastic after biofilm removal ranged from 0.82 to 0.97 g (mean 0.92 g) and the biofilm biomass ranged from 0.03 to 13.58 mg (mean 1.39 mg).

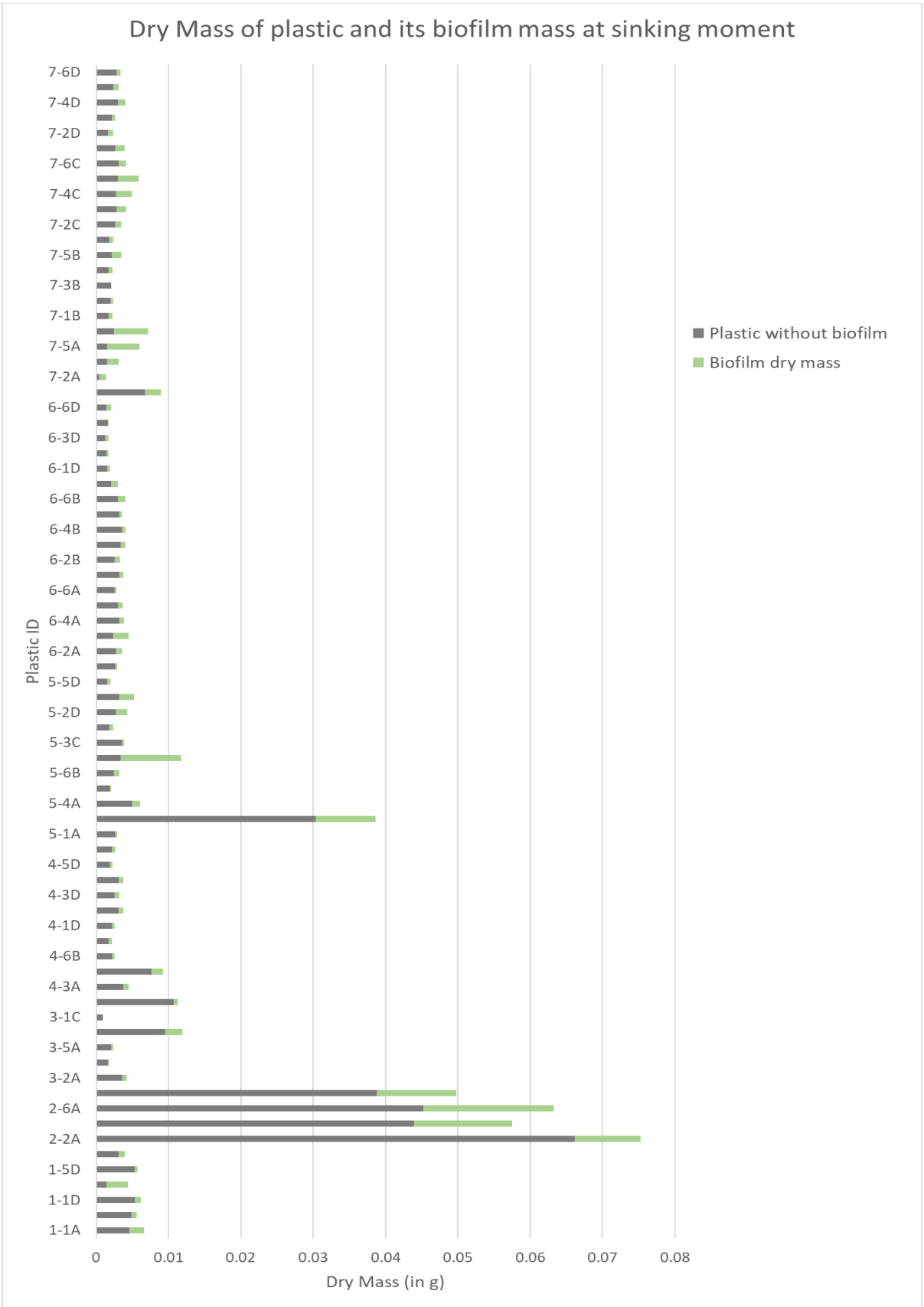


**Figure 11**. Dry mass (in g) of plastic and biofilm when the plastic reaches its sinking point. Grey: plastic without biofilm; green: dry mass of biofilm.

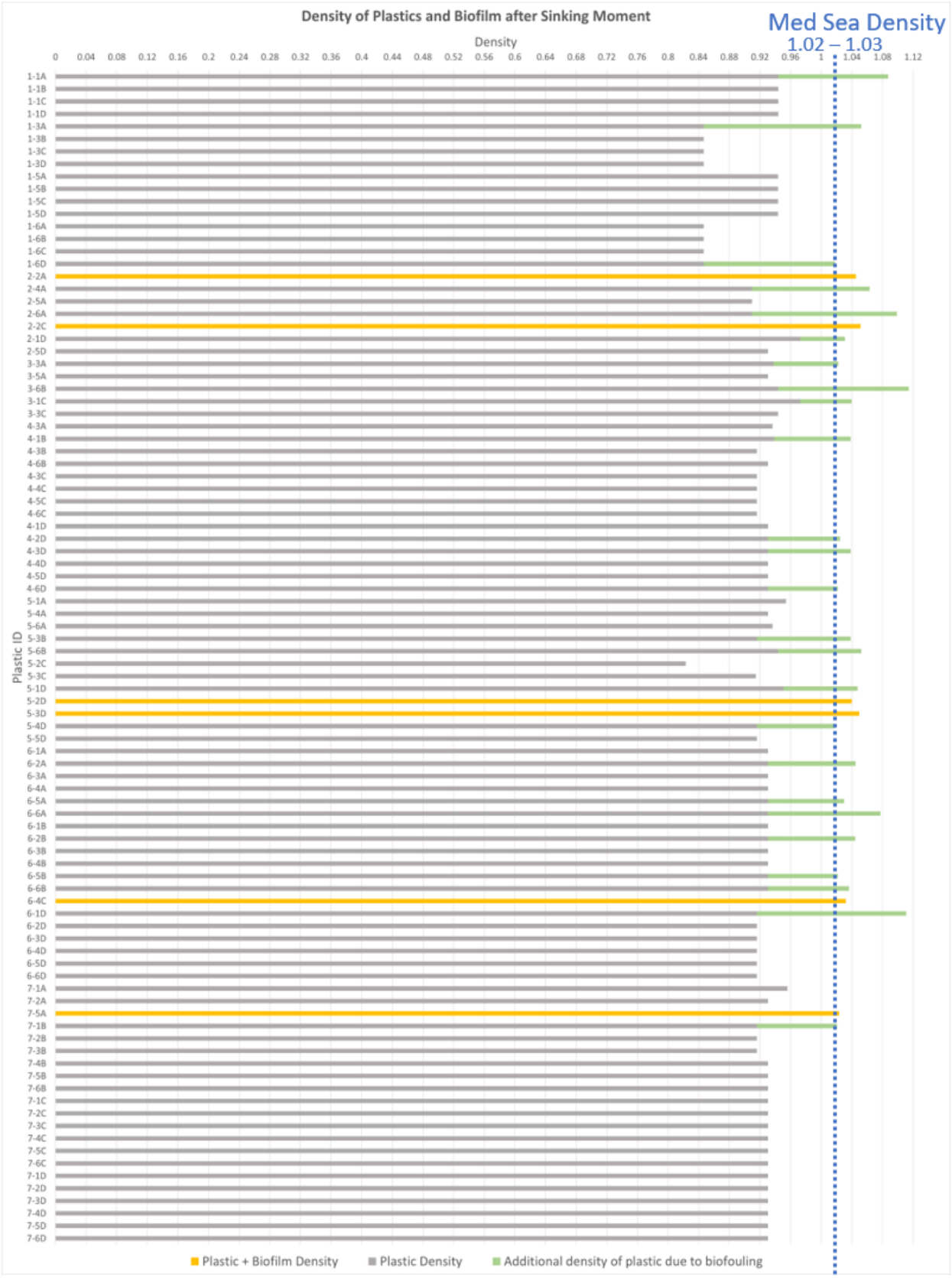


**Figure 12**. In grey, the density of floating plastics without biofilm. In light green, the extra density (due to the biofilm that was attached to the plastic). In orange, the sum of the density of the plastics and the biofilm. In blue, is the average value of the density of the seawater in the experiments.

### 3.2.3 Density of plastics

Figure 12 describes: in grey the measured density of floating plastics without biofilm. In light green, the extra density at the time they sank (average value is 0.12 +- 0.03) is represented, likely due to the biofilm that was attached to the plastic. In orange, the sum of the density of the plastics. In Blue is the average value of the seawater density in experiments that corresponds to the density of the Mediterranean seawater and varied from 1.02 to 1.03.

### 3.2.4 Rising and sinking rate of plastics

For the experiments, the plastics have distinct rise rates depending on their type, with a higher average rise rate for fragments (about 32 mm/sec) than for films (about 10 mm/sec). When data were plotted according to the surface/volume ratio there was a continuity between fragments and film behaviour. For most of the films, the experiment stops around January 2023 because they reach their sinking point in the water column (equivalent to the loss of buoyancy), Figure13.

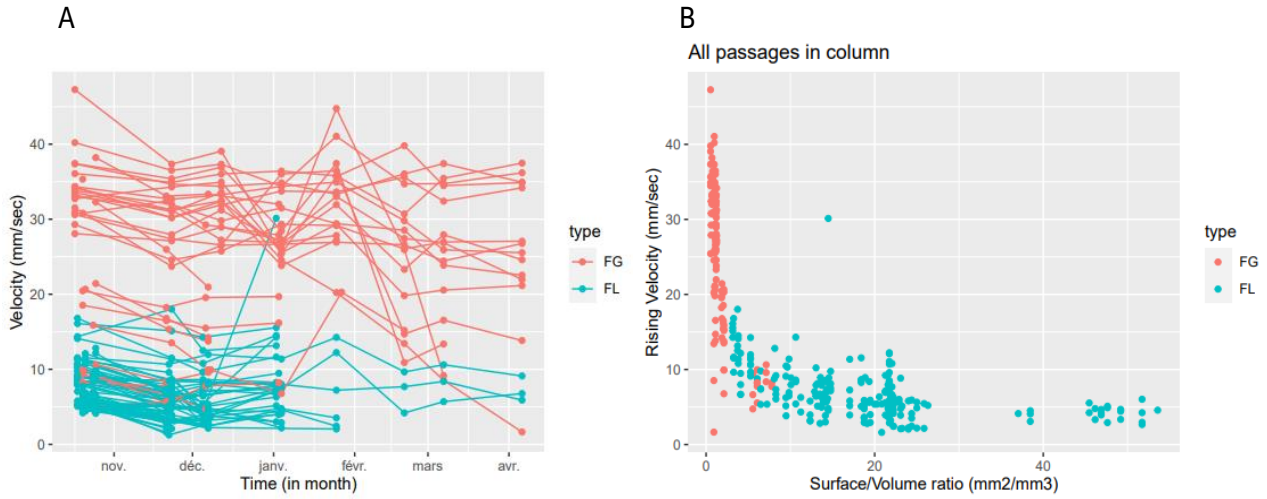


**Figure 13.** Evolution of the rise velocity of plastics. (A) as a function of incubation time and type of plastic. (B) in function surface/volume ratio and plastic type. FG: Fragments; FL: Films.

Most films reached their sinking point around December 2022 (2 months after initial incubation) while the first fragments reached this point after January 2023 (3 months of incubation) and most have not yet sunk. Sinking speed distributes in a relatively similar way as rising speed according to surface/volume ratio and plastic-type. The sinking velocity of the plastic particles varied from 0.7 to 53 mm/s (average 7.43 mm/s), Figure14.

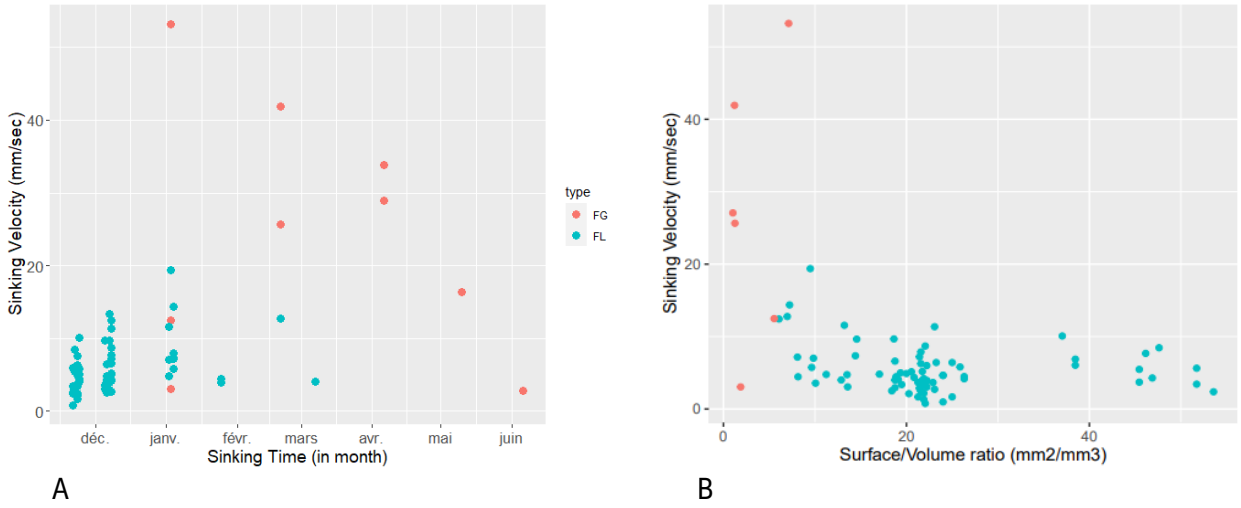


**Figure 14.** Evolution of the sinking velocity of plastics. A: as a function of incubation time and type of plastic. B: in function surface/volume ratio and plastic-type. FG: Fragments; FL: Films

### 3.2.5 Settling velocity closure

Several studies choose an experimental approach to characterize the growth and the alteration of the settling of plastics (Kaiser et al., 2017; Jalón-Rojas et al. (2022); Miao et al. (2021); and within the PLUXIN project (internal report). Other adopted theoretical frames exist (Kooi et al., 2017; Kreczak et al., 2021), applying later a settling velocity correction into larger dispersal models (Lobelle et al., 2021; Fischer et al., 2022). The common suggestion of these approaches is that the variation of the particle vertical dynamics can be explained by estimating the biofouling influence on the particle's main characteristic parameters, size, density, and shape and thus circle back towards known settling or drag closure as in the equation (8) or (10).

#### 3.2.5.1 Note on the data availability

The experiment resulted in an exhaustive data set in terms of:

→ particle number (159 fragments and films);
→ parameters being controlled (densities, wet and dry masses, size, surface, biofilm cover);
→ time dependency of the particle immersion.

This comprehensive dataset hints at an interesting analysis, especially when compared to published studies. With all data fully processed and acquired, this point, combined with the complexity of the experimental processes in terms of logistics and measurement methods, emphasizes that key data elements needed for non-dimensional analysis are now fully available.

Out of the 159 initial particles, 18 are still in the water (i.e. did not sink - mostly fragments), and 61 were lost either in the field or the laboratory before the end of their experiment (i.e. settling). 80 particles sank at the end of the experiment and had their density measured. This results in 25 particles having linked to a full dataset: settling velocities at different times with initial and final densities, biofilm cover, surface, and thickness.

These parameters (especially the density of the colonized particles) are crucial for conducting a complete non-dimensional analysis of the settling with the finding of a closure law in mind.

#### 3.2.5.2 Particles and biofilm growth characterization

Before connecting the particle settling (or rising) velocities with their colonization state, it is crucial to understand the variability of the particles that were colonized. Pictures of the particles can be found in Figure 6. Two shapes of plastics are investigated: films and fragments. In the following analysis, since different shapes have different settling behaviours, they will sometimes be addressed independently. The size distribution of the particles is given in Figure 15 with more details in Table 5.

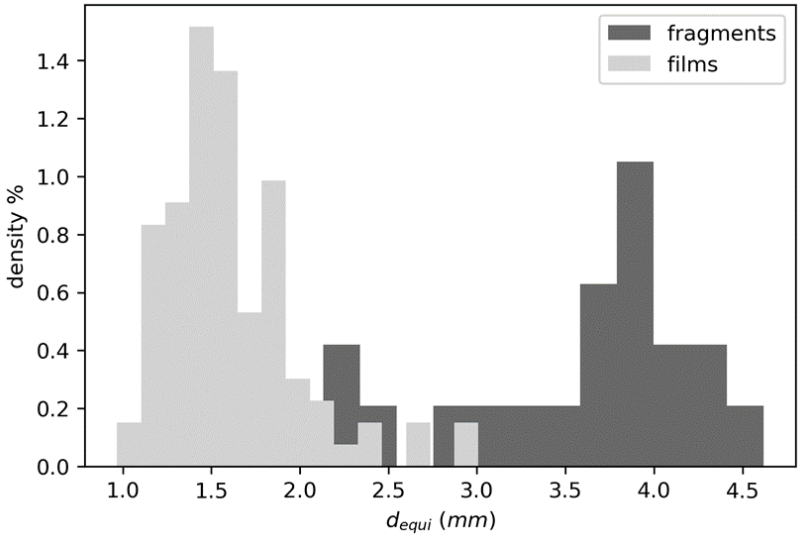


**Figure 15.** Equivalent diameter distribution for the studied particles, sorted per shapes: fragments in dark grey, films in light grey.

On the $x$-axis, the equivalent diameter ($d_e$) corresponds to the equivalent spherical diameter derived here with the available data as:

$$\boldsymbol{d_e = \sqrt[3]{surface.thickness}} \qquad \textbf{(15.)}$$

**Table 5.** *particle number, median size, shape and density*

| PARTICLES | Number of initial particles | Median equivalent diameter (mm) | Median Corey shape factor ([0-1]) | Median virgin density (kg/m³) |
|---|---|---|---|---|
| fragments | 35 | 3.70 | 0.108 | 910 |
| films | 134 | 1.52 | 0.006 | 931 |

Here, the equivalent Corey shape factor is obtained from:

$$\boldsymbol{C_{sf} = \frac{thickness}{\sqrt{surface}}} \qquad \textbf{(16.)}$$

This parameter is often used to adjust the settling velocity based on its shape for empirical closure laws as discussed before (see section 3). In this experiment, the particle shape factors remain rather small, always below 0.25 for fragments and 0.05 for films. The investigated particles are thin. This is expected to be of high importance for their settling velocities as seen in section 2.

The density of the aggregated particles is measured only twice for each particle:

→ After removing the biofilm which gives the virgin particle density: $\rho_p$

→ At the settling measurement, giving the density of the aggregate plastic + biofilm: ${\rho_p}^{bio}$

Thus, the density of the aggregated particle is unavailable for intermediary settling velocity measurements. This density is however important to look at the closure of the velocity. Methods to rebuild it based on the biofilm cover estimation have been explored. One of the methods uses a polynomial relation between the density and the biofilm cover $c$:

$$\boldsymbol{\rho(c) = \rho_p + \left({\rho_p}^{bio} - \rho_p\right)\left(\frac{c}{c_M}\right)^2} \qquad \textbf{(17.)}$$

where: $c_M$ is the biofilm cover at the settling measurement. With equation (17), it is possible to non-dimensionalize the settling velocity and the size of the particles from equations (6) and (7) and derive the drag coefficient with respect to the Reynold Number using equation (9). The variation of equivalent size of the particles due to the biofilm cover is assumed to be negligible; hence, $d_e(c) \cong d_e(c = 0\%)$.

Other evolutions of the characteristic size (based on the wet/dry masses) were investigated but are not presented here.

### 3.2.5.3 Temporal evolution of the settling velocities

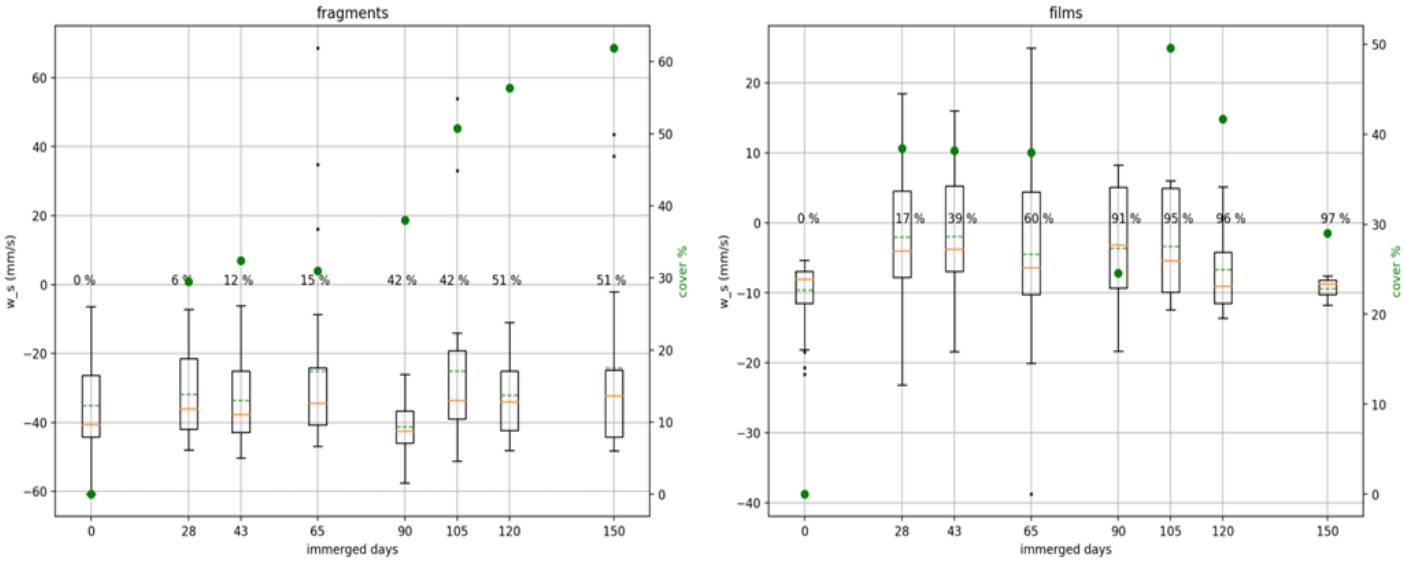


**Figure 16.** Temporal evolution of the settling velocities (left axis) with mean biological cover (right axis). The values in percent give the number of particles that settled at the time. The orange and green lines are respectively the mean and the median of the samples. Black dots represent extreme values

#### 3.2.5.4 Shape importance on the settling

The relative importance of many parameters was investigated in trying to correlate settling velocity changes with biological colonization. The main factors affecting the settling are the particle size, density, and shape including their variations with biofilm growth. Figure 17 highlights this. This figure shows the settling velocity of the virgin plastics (negative) along with their characteristic size with the shape factor in colour intensity. For both fragments and films, increasing the Corey shape factor (sphericity) relates to a greater rising velocity. Thus, finding a closure law for the biofouling on plastic with these data will first require implementing a correction for the shape of the particles.

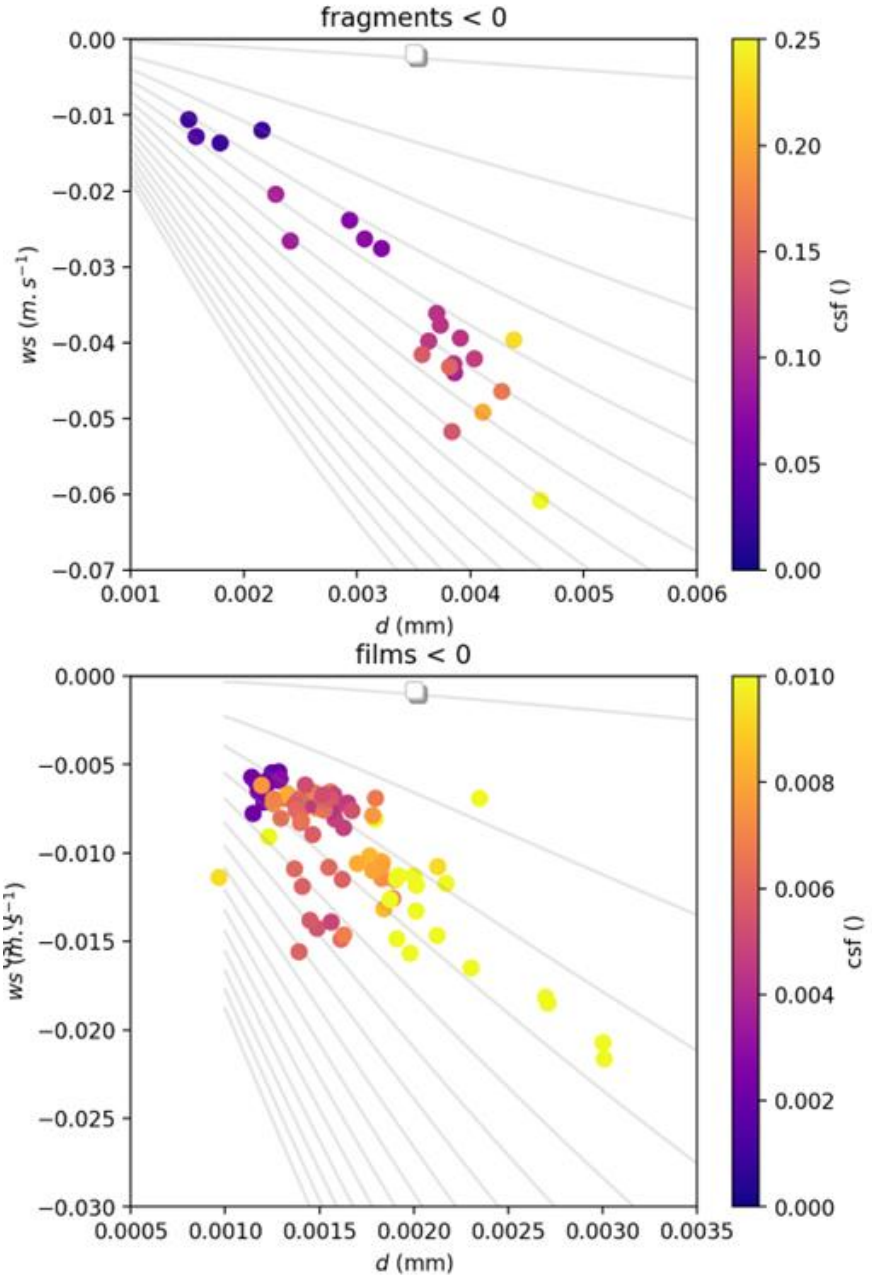


**Figure 17**. Settling velocity evolution (in m/s) with equivalent diameters (mm) for all the particles at the initial measurement. The Corey shape factor is shown as colour intensity. Top: fragments, bottom: films. Grey lines are theoretical settling velocities obtained with eq.(8), with a unique diameter and for different densities (920 g/L for the lower one to 1025 g/L for the top one).

However, as seen in Section 2, this is not a straightforward task especially considering the small value of the shape factor as known laws are generally not verified in this shape domain.

#### 3.2.5.5 Drag and Reynolds number

The settling velocities can be non-dimensionalized with equations (6) and (7), and the drag coefficient derived with respect to the Reynolds number, equation (9). The comparison with various empirical laws is shown in Figure 18 and compared to Kramer *et al.* (2021) data compilation in Figure 19.

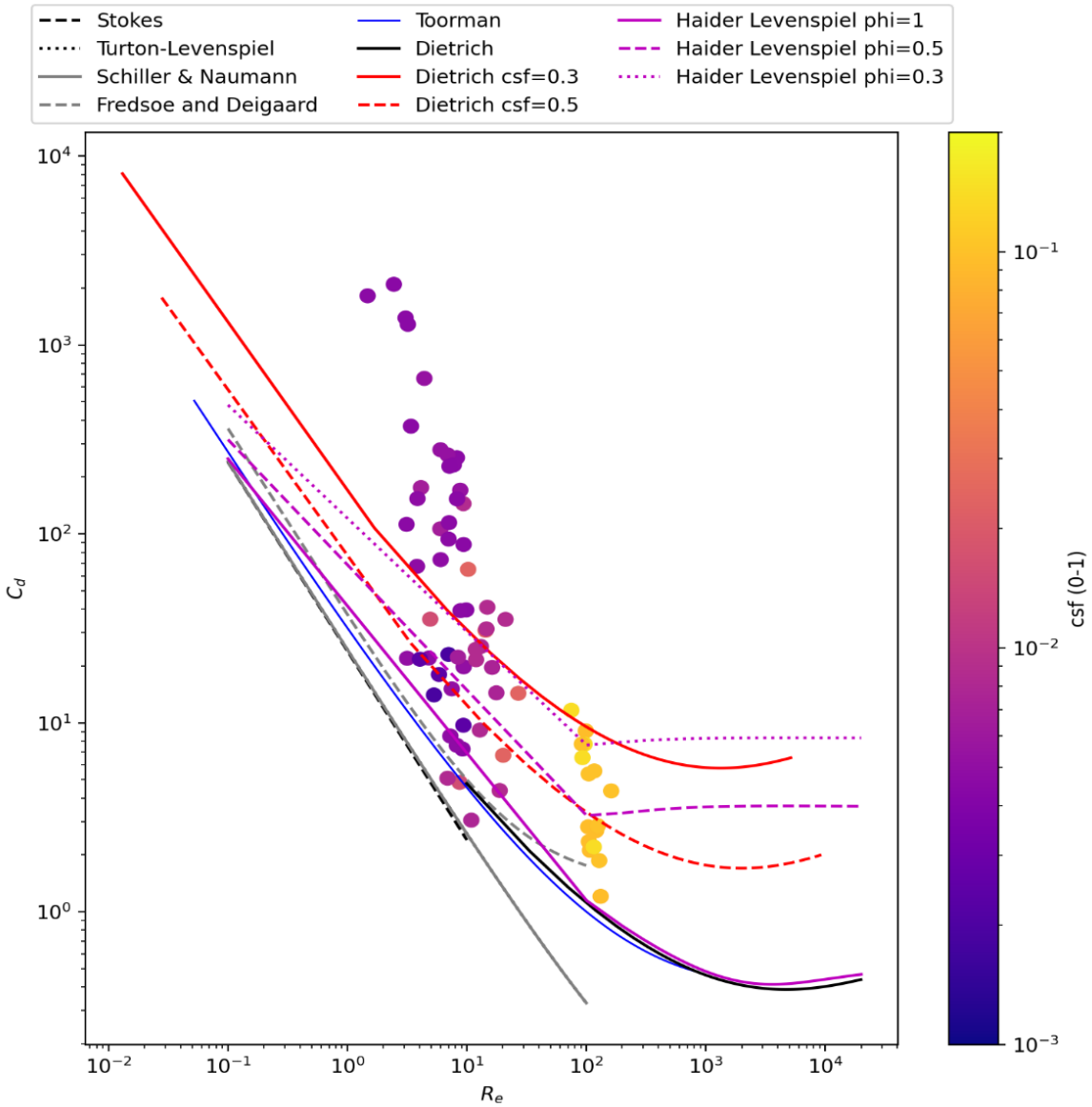


**Figure 18.** Drag coefficient in respect of the Reynolds number for several theoretical closure equations (spherical particles) and for some laws considering shape factors for the experimental settling velocities of this experiment using law (8.) and (9.). The csf is shown as colour intensity following a logarithmic scale to better highlight the small variations.

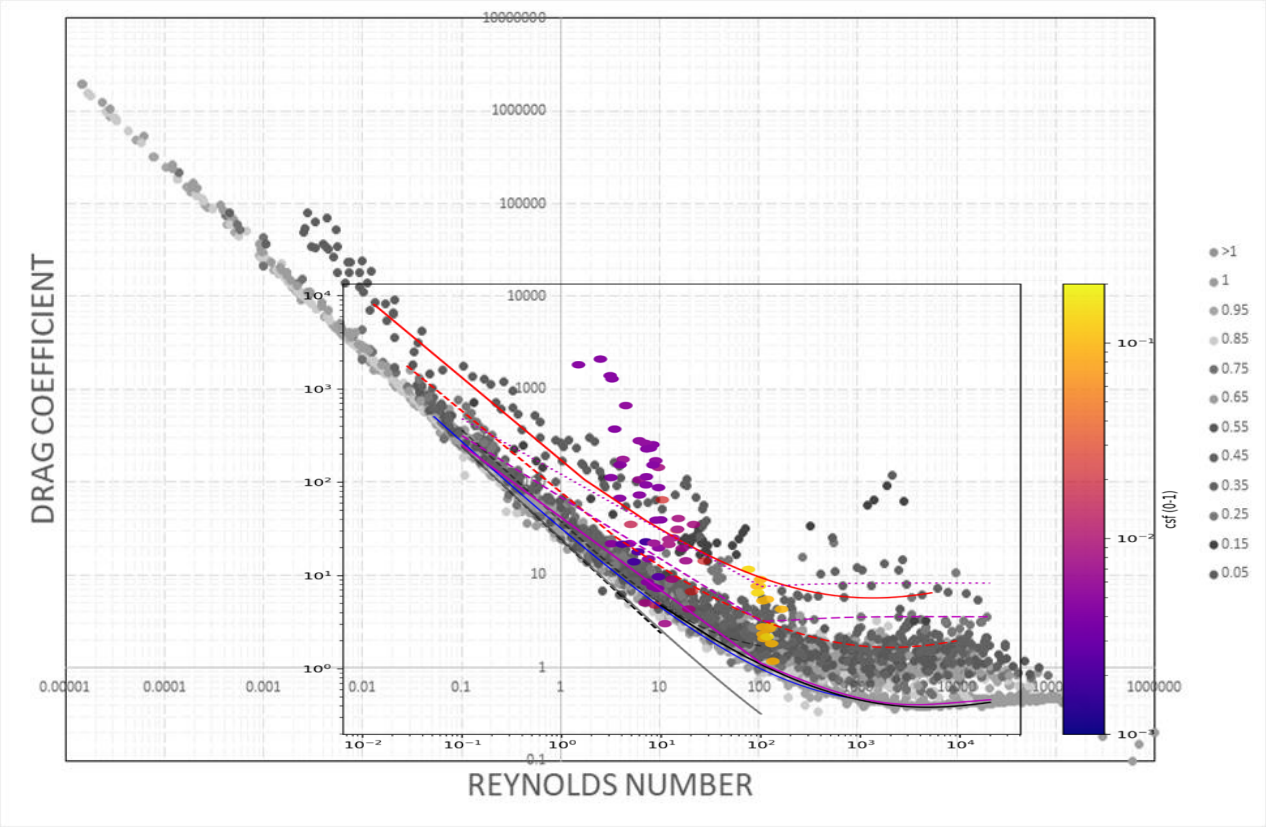


**Figure 19.** Overlay of figures 3 and 17 to emphasize the increasing scatter for decreasing shape factors.

Here again, the shape of the particles (fragments and films) appears to be the main parameter affecting changes in settling velocity. Plastic particles with similar shapes are almost aligned together with films in darker colour (smaller shape factors) and fragments in orange (larger shape factors). For the films, there seems to be a larger spread in the alignment, which could be linked to uncertainties in the settling velocity measurement method and/or to the natural variability in the settling of such a particle in relation to its shape.

The effect of biological colonization on the particles seems to be reducible to variations of the particle size, density, and shape, allowing it to circle back with established settling closures. However, in the shape range of the considered particles (thin fragments and films with low values of the shape factor), no existing closure theory allows faithful theoretical correction of the settling. We had to estimate the intermediate densities and the characteristic size of the particles at intermediary steps; different hypotheses on these parameters may lead to a better fitting of the experimental relations compared to the theory (density as a function of the wet mass, size variations).

# 4 HINDERED SETTLING CORRECTION

When many particles settle together, their motion may be hindered by that of the neighbouring particles. Water displaced by a sinking particle can increase the drag on a nearby sinking particle that "catches" this upward flow. At even higher concentrations the risk for friction and collision between particles increases. For sediments, this hindered settling correction is typically expressed in terms of the volumetric concentration $\phi$ of all suspended particles in the neighbourhood.

Eventually, the settling velocity becomes zero when the maximum packing concentration ($\phi_{max}$) is reached, i.e. for which a deposited bed is formed. For sediments, $\phi_{\max}$ typically lies in the range of 0.60-0.72, depending on the distribution of size and shape of the particles. There exist several empirical correction factors for this phenomenon. The Richardson & Zaki (1954) relationship in particular is very popular, but it fails for high concentrations. We therefore propose to use the alternative empirical closure by Toorman (1999):

$$\frac{w_s}{w_0} = \exp\left(-\frac{\phi}{\phi_1}\right)\left(1-\frac{\phi}{\phi_{\max}}\right) \qquad (18.)$$

with $w_0$ the settling velocity for an individual particle; $\phi_1 = \alpha\phi_{\max}$ ($\alpha = 0.42$ for spherical particles).

But particles also tend to cluster and fall together at a higher speed. In particular, small particles may be caught in the wake of bigger particles, by which they settle faster than on their own. Observed concentrations of plastic particles in the field are too low to expect mutual hindrance. However, the settling of plastic particles in the presence of much more abundantly present sediment particles may be hindered by the surrounding particles, no matter what their nature is. Therefore, the above equation can still be used, with $\phi$ the volumetric concentration of ALL types of particles in suspension.

# 5 SETTLING AND TURBULENCE

The characterization of the settling velocity prior to its use in numerical models is either done experimentally in still water or derived from empirical equations based on an experiment. These experiments are all done in still water. However in real flow conditions, in rivers or at sea, turbulence will be present, either due to bottom friction, local variations of the topography or external forcing such as wind or waves. This turbulence will directly affect the settling of the plastic particles.

## 5.1 The complex influence of turbulence on settling

Experimental and modelling work addressing has been debated mostly through experimental or computational studies proving either increases or reduction of the settling in turbulent flows (Zhou & Cheng, 2009; Wang et al., 2018). The total effect of turbulence on a settling particle can be explained by a combination of several effects whose importance in the settling depends on the size and density and shape (Esteban et al., 2020) of the particle compared to the turbulent temporal and spatial scales (Wang et al., 2018). First, turbulence induces fluctuation in the settling velocity, when the fluctuations are greater in the inverse direction of the settling then the particle decelerates, this is the loitering effect. Secondly, with turbulence, nonlinearity appears directly in the drag of a particle (Mei, 1993). Then, vortices can appear in turbulent flow and "trap" a settling particle. Finally, downward preferential path effects can accelerate it (Revil-Baudard et al., 2017).

What is often overlooked, is that experiments are often carried out in tanks where turbulence is generated by an oscillating grid. However, this is not so in most field conditions, where the turbulence is generated by shear flow, resulting in a different distribution of turbulence in the three orthogonal directions. Moreover, a particle

subjected to turbulent shear flow is expected to experience in addition a **lift force**, a force perpendicular to the motion of the shear flow. The contribution of a lift force can be hidden in the drag coefficient because lift and drag forces are mathematically expressed in the same way.

In addition, the particle **orientation** plays a role. It is observed that even in still water, non-spherical particles do not follow a perfect vertical path. Flat objects tend to settle in the energetically most favourable orientation, which is horizontal since it sinks then the slowest. In practice, this cannot be realized because the slightest disturbance jeopardizes this ideal situation: a flat particle would rather flutter down like a feather or autumn leaves. The fluttering is the result of the detachment of a boundary layer over the surface at one end of the particle, i.e. vortex shedding, by which the orientation of the particle suddenly changes, to move the detachment point to the other side. This explains the wiggling settling.

A stiff flat plate settling in quiescent water flutters down in a horizontal position but falls very much faster when dropped vertically, cutting the water. Hence, the orientation allows two different settling modes for the same particle, for which it is not evident to choose which one to use.

Considering in addition **flexible particles**, like fibres, filaments and foils, the shape can change continuously, with an increase of the erratic motion.

If one adds up the effect of turbulent shear flow, one can imagine that the particle's orientation can change continuously. Subsequently, the settling becomes more erratic, and the actual settling velocity can only be determined as a statistical mean over a long enough time span.

## 5.2 Experiment

In the framework of the PLUXIN project, a new experimental study has been proposed to study turbulence applied to the large polydispersity that plastic particles present and deduce general behavioural law to use in correcting the settling velocity.

### 5.2.1 Objectives

To investigate the effect of turbulence in the settling of microplastics particles, we generate turbulence in a Couette flow made of a rotating inner cylinder and a fixed outer cylinder (Figure 20). When the rotating speed of the motor is important enough, the inner cylinder will generate a circular turbulent flow. Then modification of the settling velocity of MP can be observed using recording and particle tracking algorithms.

### 5.2.2 Methods and measurements: Couette flow

#### 5.2.2.1 Set up and theory

The inner cylinder can rotate on its axis driven by an electrical motor. The rotation speed goes from 0-100 rpm. At a defined rotation speed $\omega$, the rotation drags along the initially still surrounding water creating a circular turbulent flow: a Taylor-Couette flow.

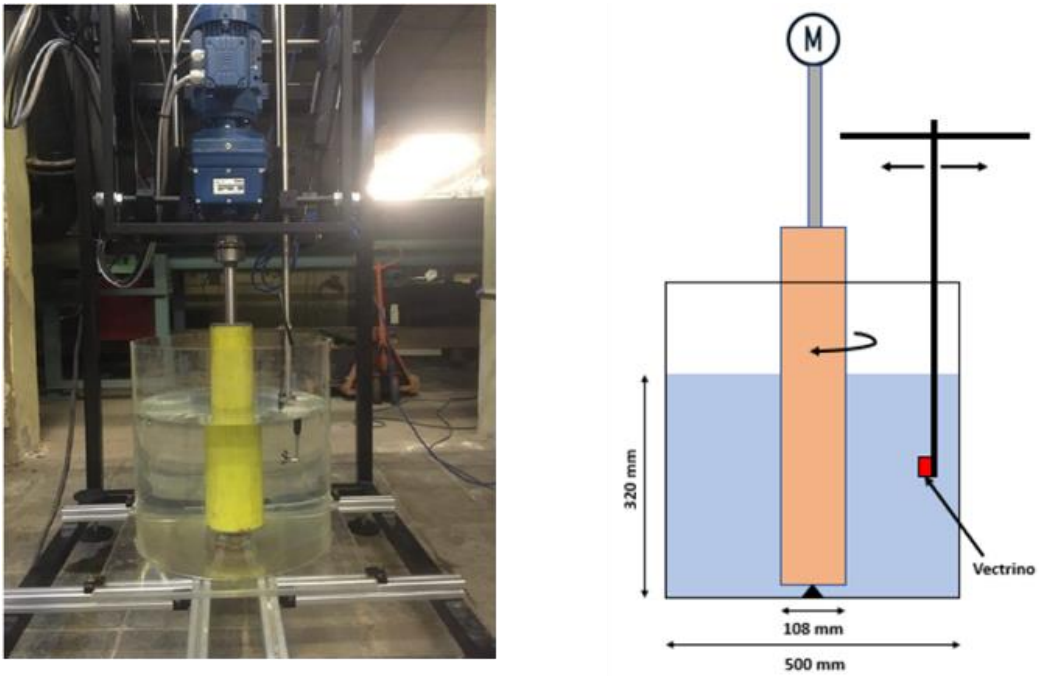


**Figure 20.** Photograph (left) and schematic representation (right) of the circular flume, with the inner and outer cylinder (yellow and transparent plexiglass), the motor (blue) and its supporting frame (black). The Vectrino profiler is visible both in the photograph and in the schematic representation.

The steady-state theoretical angular velocity at any radial position $u_\theta(r)$ in the flume is well known and follows a logarithmic profile from the inner to the outer cylinders (Berlamont, 2006):

$$\boldsymbol{u_\theta(r) = \omega R_1 - \frac{u_*}{\kappa} \ln\left(\frac{r - R_1 + \xi_0}{\xi_0}\right)} \qquad \textbf{(19.)}$$

with $u_* = \frac{\kappa \omega R_1}{ln\left(\frac{R_2 - R_1 + \xi_0}{\xi_0}\right)}$ the friction velocity, $R_1$ and $R_2$ respectively the inner and outer cylinder radius, and $\xi_0$ is an optimization parameter.

#### 5.2.2.2 Methodology

A Nortek ADV profiler is used to measure the flow velocity at different depths of the water. This device is attached to a frame that can glide vertically and in the radial direction of the flume allowing velocity measurement at different depths and radial positions. Measurements are done at different positions and over 1 minute duration to be able to derive the instantaneous variations of the velocity and hence, the turbulence. The profiler measures over a given duration the velocity over a depth of 3cm. Results are filtered to keep only significant data.

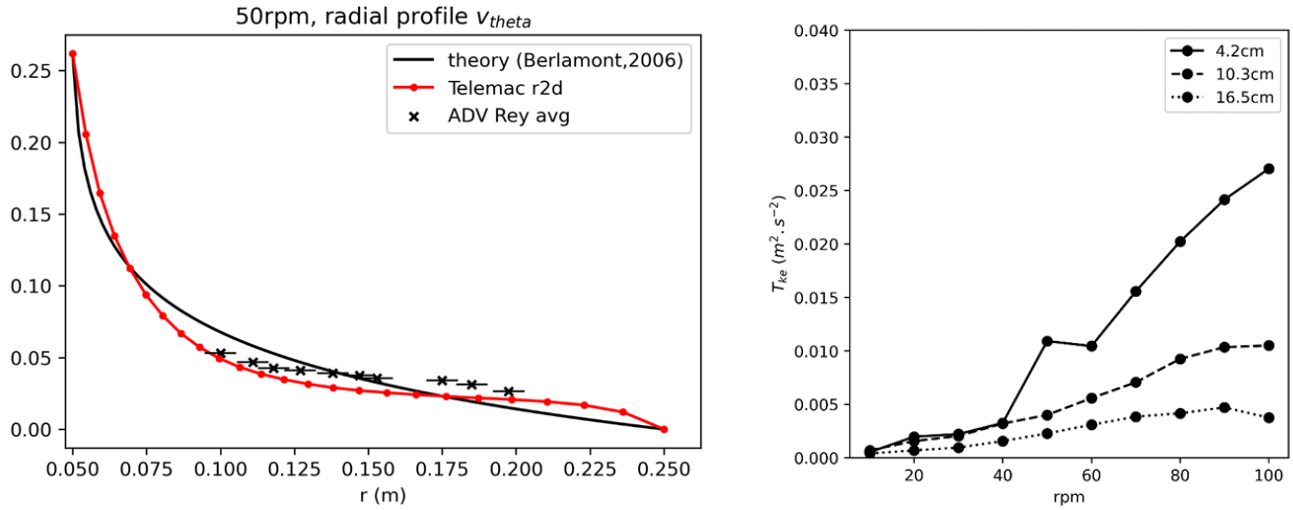


**Figure 21.** Left is the radial velocity profile from equation (19.) at 50 rpm, from theory (black) measurements (crosses) and numerical simulation (red) with a Telemac2D model of the flume. On the right is the turbulent Kinetic Energy of the water for different rotational speeds and at 4.2, 10.3 and 16.5 cm from the centre of the tank.

The turbulent regime of such a Taylor Couette flow is rather complex to describe as it involves initially turbulent structures being created before transitioning to a fully turbulent regime. The Taylor number, $T_{ke}$, can be used to characterize the state of these turbulent structures. Here, we propose to study the evolution of the turbulent kinetic energy at three radial locations of the flow (4.2, 10.3 and 16.5 cm from the inner cylinder) with respect to the inner cylinder rotating speed. This factor characterizing the turbulence in the three directions was obtained as follows:

$$\boldsymbol{T_{ke,i}} = \mathbf{0.5}\sqrt{\boldsymbol{u_{r,i}}'^2 + \boldsymbol{u_{\theta,i}}'^2 + \boldsymbol{u_{z,i}}'^2} \qquad \textbf{(20.)}$$

where $u_{r,i}'$, $u_{\theta,i}'$ and $u_{z,i}'$ are the instantaneous turbulent velocities deduced from the Reynolds decomposition of the velocity over the measurement period. $i$ represents the vertical position from the profiler measurement. The general energy is the average energy over the vertical.

$$\boldsymbol{T_{ke}} = \sum_{\boldsymbol{i=1}}^{\boldsymbol{N}} \boldsymbol{T_{ke,i}} \,/\, \boldsymbol{N_{mes}} \qquad \textbf{(21.)}$$

### 5.2.3 Settling velocity

#### 5.2.3.1 Methodology

Plastic particles are dropped at the surface (or released from the bottom) and their settling (or rising) is recorded using a camera on the side of the tank. This is repeated several times for each particle and each rotating speed allowing to account for the variations of the settling from one repetition to another. Particle settling velocities are then derived numerically using a particle tracking algorithm developed with the python module Trackpy.

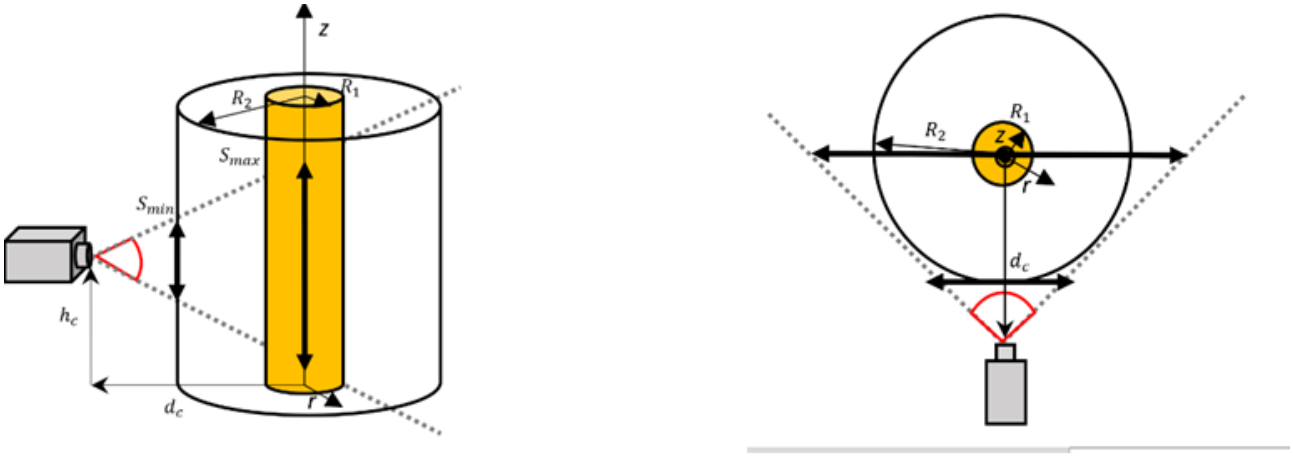


**Figure 22**. Schematic representation (top (right) and side (left) view) of the recording device with the flume and the horizontal depth issue that arises with only one point of view.

#### 5.2.3.2 Results

The experiment has been carried out to this end, for a single spherical particle with a diameter of 1 mm made of clear PET to facilitate the particle recognition in the algorithm. The evolution of its settling velocity with the inner cylinder speed is shown in Figure 23.

Figure 23 shows that there seems to be a decrease in the mean and median settling velocity with increased turbulence, but this decrease is smaller than the variance. This experiment would need to be repeated for many particle sizes and shapes to produce a more significant data set to analyse. With this setup, the analysis method, and especially the derivation of the settling velocity (settling between planes $S_{min}$ and $S_{max}$ in Figure 22) results in a large scatter in the velocity. Thus, it is difficult to link the turbulence on the path of the particle to changes in its settling. As shown in Figure 21, the turbulent intensity decreases rapidly from the inner cylinder to the outer cylinder. Thus, in exploring this experiment further, the use of particle image velocimetry is recommended to be investigated for future research.

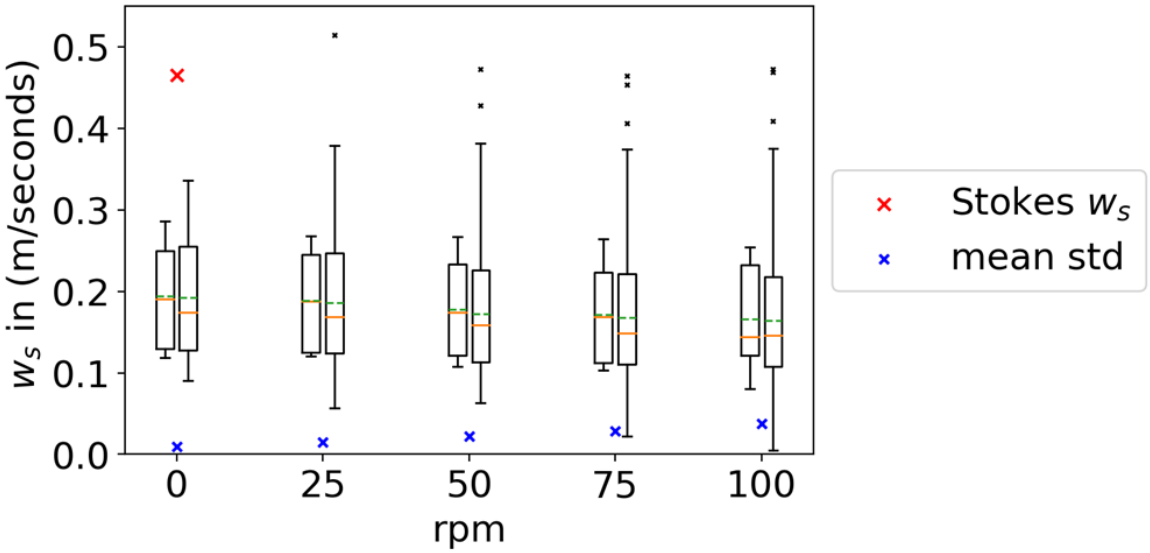


**Figure 23.** Settling velocity of the particle according to the rotating speed of the inner cylinder. The Mean standard deviation of the velocity from its mean is also presented in blue. The left boxes are the averaged velocity distribution of each settling repetition. The right boxes show the instantaneous settling velocity. orange lines are the median while green lines are the mean.

# 6 HETERO-AGGREGATION

Hetero-aggregation refers to the aggregation of MP particles (bio-fouled or not) with other ambient particles in water, in particular with the much more abundantly present sediment and organic matter particles. This aggregated particle will once again present altered size and buoyancy due to size, shape, and density variations.

**Remark:** Microplastics can in principle also aggregate with each other – homo-aggregation –, especially when small in size (increasing the surface charge effects) and biofouled, but the number concentration of plastics is usually so small that the probability of occurrence of homo-aggregation is so small that it can be neglected.

## 6.1 Cohesive sediments flocs

Among the particles in rivers and at sea, flocs of cohesive sediments are suggested to be the main type of particle significantly allowing aggregation of plastic particles and affecting their vertical distribution. Cohesive sediment particles tend to assemble together and form larger aggregates. These flocs can further develop in size by either aggregating further with other suspended matter or breaking down into smaller pieces due to external forcing (shear, turbulence or collision). The settling of cohesive sediments must thus consider this effect as it will largely impact the sizes, shapes and density distribution of cohesive sediments. MP could be trapped inside these flocs which will as well alter their settling.

## 6.2 Experimental observations of altered MP settling with flocs

The interaction between MP and suspended sediment in water has been recently explored through several experiments. These experiments, mostly in laboratory settings, tested the effect of MP and cohesive sediments on the general settling of MP through different combinations of plastic particle types (buoyant and settling) with different kinds of suspended matter and sediments and hence floc sizes. According to these studies, aggregation in flocs tends to happen when the floc size is greater than the plastic particle (Leiser et al., 2021). Once aggregated the settling velocity of the plastic-sediment aggregate is modified. Buoyant plastic particles were shown to settle with the suspended sediments inducing a general reduction of the floc settling velocity (Laursen et al., 2021; Leiser et al., 2022). While already settling plastics were shown to settle faster with the mix (Andersen et al., 2021; Leiser et al. 2022; Li et al., 2019).

## 6.3 Correction of MP settling in flocs

The particle transport models developed in the framework of the LABPLAS project include as suspended matter two types of sediments: non-cohesive (sand) and cohesive sediments (mud). The vertical transport of the cohesive sediments will be characterized by modification of primary particles settling velocity following a flocculation model developed at the KU Leuven Hydraulics Laboratory (Escobar et al., 2023). It is possible to envision modification of the settling velocity of trapped plastic particles using the settling velocity of these flocs. Currently, the assumption that is done in the plastic dispersal model is that trapped plastic settles with the cohesive sediment flocs without modifying their settling velocities. This assumption follows from the significantly larger mud concentration in the water compared to plastic litter.

To match the reality better, the plastic particles trapped in the sediment should be removed from the free plastic population as a sink term in its mass balance. The likeliness that these particles can be released again when flocs break up is assumed to be negligibly small since it is more likely that they reach the bottom. This assumption simplifies the computations since otherwise, the trapped particles have to be traced separately.

# 7 Determination of the Representative Settling Velocity of a Particle Cloud

So far, the focus was on the settling velocity of an individual particle, and the parameters which control it. However, we have to face the reality that plastics in the aquatic environment are a mix of different particles, each with its own characteristics. It is impossible to track the many particles individually. To reproduce the net effect of particle dispersal in the aquatic environment by a particle transport model, one should be able to determine the representative settling velocity of the entire population of particles in each location of the studied area. This is not trivial, since each particle may have a different density, size and shape, the three key parameters which determine the fall velocity of an individual particle.

## 7.1 Size distribution

As described already in the previous sections, the size of the plastic particle has a greater impact on the settling velocity with which it will move vertically in the water column. The relationship between settling velocity and particle diameter is evident in equations (1) to equation (4) under section 1. In addition to this, the density variations occur due to the biofilm growth and/or due to the effects of the sediment flocs. Before dealing with these complex bio-geo-chemical processes, the polydispersity in the settling velocity arising from the size distribution of a particle population needs to be addressed in the modelling of plastic transport. In the Eulerian discrete classes (DC) method, for each different property of the plastic, a different particle class must be defined. To model a wide size range – from a few micrometres to a few millimetres – several size classes must be defined requiring high computational resources.

In the framework of the Flemish PLUXIN project (www.PLUXIN.be), a novel approach of the Population Balance Equation (PBE) method on the size distribution of the plastic population is proposed (Figure 24) where discrete classes are avoided by using statistical quantity namely moments of the size distribution. This work was completed under the current LABPLAS project (Shettigar *et al.*, 2024).

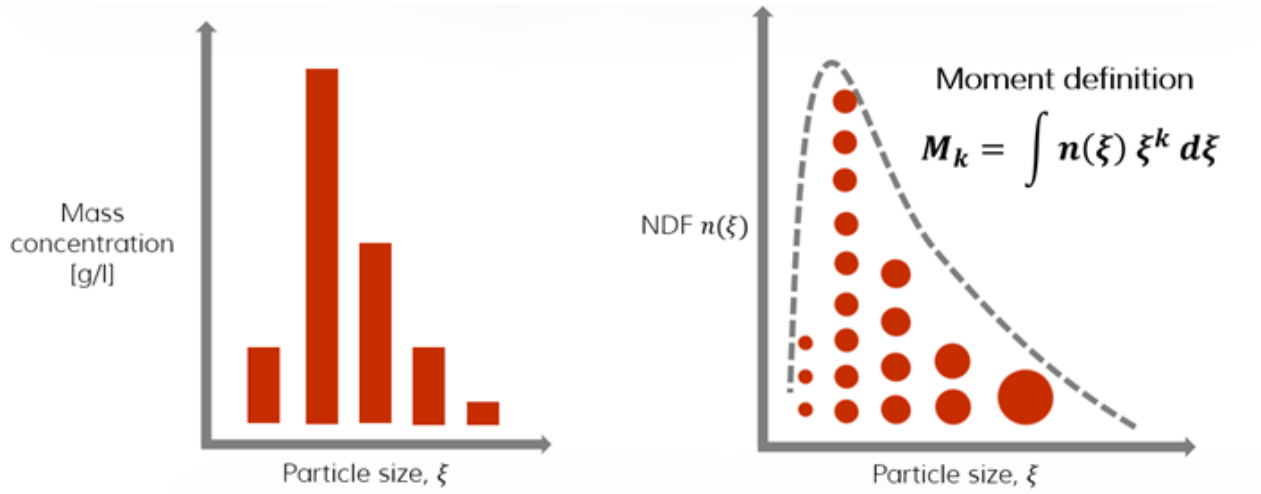


**Figure 24.** Concept of discrete class (DC - left plot) and population balance equations (PBE - right plot) modelling approaches. The DC model uses mass concentrations corresponding to different size classes. In PBE, moment values of the normalized distribution function (NDF) are used in the transport equation (Shettigar et al., 2024).

The mathematical expression of PBE applied to a system with a particle population in a carrier fluid consists of the momentum conservation (i.e. Navier-Stokes) equations (or other shallow water simplification) for the carrier fluid and a transport equation with advection and diffusion terms, source terms (e.g., dissolution, deposition), integral terms (e.g. aggregation and breakage) for the particle population.

Several methods of solving PBE can be found in the literature. The class or sectional method works by discretizing the internal coordinate space into intervals (classes or sections), transforming the PBE into a set of macroscopic balance equations in the physical domain. However, a large number of scalars (i.e., classes) are required to maintain reasonable accuracy. An effective and more elegant solution is found through the Method of Moments (MoM). A discrete set of moment values carries the normalized distribution function (NDF) information. The lower-order moment values are related to the mean, variance, skewness, and flatness of the statistical distributions described by the NDF. MoM is appropriate for use with computational fluid dynamics (CFD) codes because the internal coordinates are integrated, requiring only a small number of scalars (i.e., lower-order moments) at each grid point. In the case of a single internal coordinate which assumes only $\mathbb{R}^+$ (non-negative real numbers), the moment expression reduces to:

$$\boldsymbol{M_k}(\boldsymbol{x},\boldsymbol{y},\boldsymbol{t}) = \int_0^{+\infty} \boldsymbol{n}(\boldsymbol{\xi};\ \boldsymbol{x},\boldsymbol{y},\boldsymbol{t})\ \boldsymbol{\xi^k}\ \mathbf{d}\boldsymbol{\xi} \qquad \textbf{(22.)}$$

where: $n(\xi;\ x,y,t)$ = number density function [number/m$^3$] or [1/m$^3$]; $\xi$ = internal coordinate of NDF e.g. particle size; $x, y$ = spatial coordinate; $t$ = time coordinate;

The lower-order moment values are plugged into every term of the particle transport equation replacing the concentration values of discrete classes. The solution of such a moment transport equation provides the moment evolution over time and space instances. The moment values are then used to reconstruct the full particle size distribution using moment inversion algorithms, where moment values are transformed into respective weights and abscissae. The abscissas $\xi_i(x,y,t)$ and the weights $w_i(x,y,t)$ are derived from the lower-order moments utilized in the transport equation. The NDF is then approximated with the discrete weighted sum of Dirac $\delta$ functions and with previously determined weight and abscissa values as follows:

$$\boldsymbol{n}(\boldsymbol{\xi};\ \boldsymbol{x},\boldsymbol{y},\boldsymbol{t}) \approx \sum_{\boldsymbol{i=1}}^{\boldsymbol{N}} \boldsymbol{w_i}(\boldsymbol{x},\boldsymbol{y},\boldsymbol{t})\ \boldsymbol{\delta}[\boldsymbol{\xi} - \boldsymbol{\xi_i}(\boldsymbol{x},\boldsymbol{y},\boldsymbol{t})] \qquad \textbf{(23.)}$$

The knowledge of the particle size distribution $n(\xi;\ x,y,t)$, can be used to determine the mean size values and subsequently mean settling velocity is determined as formulated in section 2. The mean settling velocity found through this approach is controlled by the hydrodynamics of the system i.e., the heavier particles are found in abundance in the deposited material and lighter particles are found more in suspension. This avoids the use of a user-defined constant settling velocity as in the conventional class-based methods. The mean particle size is used for better estimation of the plastic erosion and deposition fluxes as in the classic sediment mechanics case. Further, the mean settling velocity could be adapted to the cases where sediment flocculation and/or the biofouling effects are to be considered. In the case of sediment flocculation, the settling velocity of the particle can be chosen between the mean ling velocity from the NDF and the floc settling velocity with a predefined criterion. In the case of biofouling, the settling velocity closure found through the experimental data and analysis (section 3) would be used. These are the further developments to be carried out in both the LABPLAS project and project PLUXIN.

## 7.2 Correction for degradation and break-up

Following the studies on weathering of plastics, we will assume that the resulting change in density remains negligibly small. However, the fragmentation into smaller pieces has to be taken into account.

Following the aforementioned methods in addressing the effect of the size distribution on the settling of MP, changes in this distribution by degradation can be approached with the same method for both approaches DC and PBE. This process will directly affect the distribution of the plastic for the two cases (DC and PBE). The degradation could follow different mechanisms not explored here, the final settling velocity of the plastic will be deduced from the characteristic settling velocity of the degraded size distribution that is defined differently for DC and PBE.

Fragmentation may be occurring faster due to mechanical shear (e.g. for beached plastics with sediments) of the break-up of floating plastics by ship propellers. The latter can roughly be estimated by making use of databases on shipping traffic densities.

Degradation and break-up time scales (>years) may be too long for correction considering the effect to induce significant variations in the dispersal model results, especially compared to the other phenomena discussed in this report (biofouling, hetero-aggregation).

Moreover, the age of each particle in a local mixture of plastic particles can be expected to vary widely. At this moment, no proven technique exists to determine the age and degree of degradation of plastic. Therefore, it is meaningless to explicitly take this into account.

## 7.3 Dealing with the heterogeneity of plastics

More generally, a sample of plastics from the field consists of a heterogeneous mix of different particles, with variability in polymer composition (thus density), size, shape, degree of biofouling and degradation. In principle, the PBE technique should be extended from the single parameter of size to the other parameters (density and shape) as well, with biofouling and degradation taken into account in the kinetics equations. But for the latter time-dependent processes, we usually do not know the age of the particles and/or the rate of the kinetics. The development of such a multi-parameter PBE method would require a lot of data to obtain statistically significant information. Unfortunately, so far, the sample processing techniques are too slow and the sample sizes (numbers of particles per sample) too small and too diverse (even in the same location), that this remains an impossible task at this moment.

A potentially more feasible short-cut could be a more pragmatic solution in defining directly a distribution function for the settling velocity (provided that we know either, size, shape and density of each particle to compute the settling velocity of each particle from one of the above equations, or that it is measured).

# 8 CONCLUSIONS

This deliverable, based on theoretical and experimental work, provides crucial information on the closure of the multi-parameter settling velocity of microplastic particles in aquatic environments. The research focused on several key factors influencing the transport of microplastics, including inertia, shape, biofouling and turbulence, as well as the hetero-aggregation of microplastics with other particles.

The terminal settling velocity (or fall velocity - including rising, which corresponds to negative values) is the most important parameter to predict the transport of particles by flowing water. It is a particle property which depends on the size, the difference in density between the particle and the ambient fluid, the shape, the total volumetric concentration of *all* particles present (including sediment and biogenic particles), and the amount of biofouling.

The settling velocity of an individual particle is most elegantly described by the Turton & Clark (1987) formula (eq.8), whose coefficients can be expressed in terms of one or more shape parameters.

In the absence of settling velocity data, it is recommended to use the following formula of the form of eq.(8) for direct calculation of the settling velocity for particles with an average Corey shape factor $C_{sf} = 0.7$ as representative for the entire plastic population:

$$\boldsymbol{w_p = \left(\left(\frac{\rho_p}{\rho_f} - 1\right) g \nu\right)^{1/3} \left(\left(\frac{4}{3}\frac{{d_*}^2}{A}\right)^{-1} + \left(\frac{\sqrt{d_*}}{\alpha}\right)^{-1}\right)^{-1}} \qquad \textbf{(24.)}$$

with $A = 32$, $\alpha = 0.86$ , $n = 1$ (already replaced), and $d_*$ the non-dimensionalized particle size, computed as:

$$\boldsymbol{d_* = d\left(\left(\frac{\rho_p}{\rho_f} - 1\right)\frac{g}{\nu^2}\right)^{1/3}} \qquad \textbf{(25.)}$$

This corresponds well with the fit of Cheng's (1997) proposal for natural granular particles (like sand) with the same shape factor. In general, the value of the three parameters in this relation increases ($A$, $\alpha$ and $n$) with shape decreasing shape factor. Considering the huge scatter in the experimental data, the determination of these empirical relationships, in particular for low sphericity, is left for future research.

Shape effects are extremely important and explain the wide uncertainty on the actual value of the settling velocity. A compilation of experimental data shows that repeated experiments with the same particle result in different mean values, since the particle spins during its fall during which the vortex separation points move from place to place, leading to an unsteady vertical motion. It is found that the uncertainty band increases with the non-dimensionalized particle size $d*$ (or with $\mathrm{Re}_p$), i.e. with increasing boundary layer turbulence production. The uncertainty bandwidth is one order of magnitude, O(10), for more or less granular particles (Corey shape factor > 0.4), two orders of magnitude, O($10^2$), for flattened particles (0.4 > Corey shape factor > 0.1) and three orders of magnitude, O($10^3$), for strongly elongated, fibre-like particles (Corey shape factor < 0.1).

The fall velocity is determined in still water. In flowing water, particles are subject to additional net turbulent lift and drag by currents and the shear flow turbulence generated by the corresponding velocity field. This will reduce the effective rate of vertical motion. Flat particles and foils are the most susceptible to drag by currents.

For particles smaller than 2 µm (i.e. colloidal particles) the effect of gravity becomes negligible and Brownian motion is the dominant mechanism. They can be modelled as passive tracers.

Effects of biofouling and turbulence are found to be of minor importance relative to the uncertainty band on the settling velocity calculation. Moreover, biofouling has a unique history for each individual particle. Therefore, it has no meaning to include it explicitly, as no model can trace all the particles individually.

To take into account the hindrance effect of neighbouring particles, the individual particle settling velocity can be corrected with a hindered settling correction factor, expressed in terms of the total volumetric concentration of all particles present in the direct neighbourhood of the point corresponding to the computational node.

It is recommended to take into account the variability in particle properties by the implementation of a probabilistic approach. The Population Balance Method has been proven to be a promising tool (Shettigar *et al.*, 2024). Because of the many parameters affecting the transport, a size-based method is not sufficient. A settling velocity based method seems to be the most promising approach, which is expected to become realized in the near future.

## REFERENCES

Andersen, T.J., Rominikan, S., Olsen, I.S., Skinnebach, K.H., Fruergaard, M. (2021). Flocculation of PVC microplastic and fine-grained cohesive sediment at environmentally realistic concentrations. The Biological Bulletin, 240(1), 42-51.

Baba, J., Komar, P.D. (1981). Measurements and analysis of settling velocities of natural quartz sand grains. J. Sediment. Petrol., 51, 631– 640.

Bagaev, A., Mizyuk, A., Khatmullina, L., Isachenko, I., Chubarenko, I. (2017). Anthropogenic fibres in the Baltic Sea water column: field data, laboratory and numerical testing of their motion. Sci. Total Environ., 599–600, 560–571.

Briggs, L., McCulloch, D., Moser, F. (1962). The hydraulic shape of sand particles. J. Sediment. Petrol., 32(4), 645–656.

Camenen B. (2007). Simple and general formula for the settling velocity of particles. J. Hydraul. Eng., 133(2): 229-233.

Characklis, W.G. (1991). Biofouling: effects and control. In Biofouling and Biocorrosion in Industrial Water Systems: Proceedings of the International Workshop on Industrial Biofouling and Biocorrosion, Stuttgart, September 13–14, 1990 (pp. 7-27). Springer Berlin Heidelberg.

Cheng, N.S. (1997). Simplified settling velocity formula for sediment particles. J. Hydr. Eng., 123(2):149-152.

Clift, R., Gauvin, W.H. (1970). The motion of particles in turbulent gas streams. Proc. Chemeca '70, Australian National Committee of the Institution of Chemical Engineers and the Australian Academy of Science (Melbourne and Sydney, Australia, August 1970).

Corey A.T. (1949). Influence of shape on the fall velocity of sand grains. PhD thesis, Colorado State University, Fort Collins, CO.

Dallavalle, J. (1948). Micrometrics: The Technology of Fine Particles, Pitman, London.

Dietrich, W. E. (1982). Settling velocity of natural particles. Water Resources Research, 18(6), 1615-1626.

Digouardi F., Mele D. (2015). A new shape dependent drag correlation formula for non-spherical rough particles. Experiments and results. Powder Technology, 277.

Digouardi F., Mele D., Dellino P. (2018). A new one-equation model of fluid drag for irregularly shaped particles valid over a wide range of Reynolds number. J. Geophysical Research: Solid Earth, 123, 144–156.

Escobar, S., Bi, Q., Fettweis, M., Wongsoredjo, S., Monbaliu, J., Toorman, E. (2023). A dynamic 2DH flocculation model for coastal domains. Ocean Dynamics (in press).

Esteban, L.B., Shrimpton, J.S., Ganapathisubramani, B. (2020). Disks settling in turbulence. J. Fluid Mechanics, 883, A58.

Fazey, F.M., Ryan, P.G. (2016). Biofouling on buoyant marine plastics: An experimental study into the effect of size on surface longevity. Environmental Pollution, 210, 354-360

Fischer, R., Lobelle, D., Kooi, M., Koelmans, A., Onink, V., Laufkötter, C., ... van Sebille, E. (2022). Modelling submerged biofouled microplastics and their vertical trajectories. Biogeosciences, 19(8), 2211-2234.

Gall, S.C., Thompson, R.C. (2015). The impact of debris on marine life. Marine Pollution Bulletin, 92(1-2), 170-179.

GESAMP (2015) Sources, fate and effects of microplastics in the marine environment: a global assessment. Kershaw PJ (ed). Rep Stud GESAMP No. 90, 96 pp

Geyer, R., Jambeck, J.R., Law, K.L. (2017). Production, use, and fate of all plastics ever made. Science Advances, 3(7), e1700782.

Haider, A., Levenspiel, O. (1989). Drag coefficient and terminal velocity of spherical and nonspherical particles. Powder Technology, 58(1), 63-70.

Hallermeier R. (1981). *Terminal settling velocity of commonly occurring sand grains*. Sedimentology, 28(6), 859-865.

Hoerner S.F. (1965). Fluid Dynamic Drag. Bakersfield (CA): Hoerner Fluid Dynamics.

Hölzer A., Sommerfeld M. (2008). New simple correlation formula for the drag coefficient of non-spherical particles. Powder Technology 184, 361-365.

ISO, P. (2019). 1183-1; Plastics—Methods for Determining the Density of Non-Cellular Plastics—Part 1: Immersion Method, Liquid Pycnometer Method and Titration Method. PKN: Płock, Poland.

Jalón-Rojas, I., Romero-Ramírez, A., Fauquembergue, K., Rossignol, L., Cachot, J., Sous, D., Morin, B. (2022). Effects of biofilms and particle physical properties on the rising and settling velocities of microplastic fibers and sheets. Env. Science & Technology.

Jambeck, J.R. et al. (2015). Plastic waste inputs from land into the ocean. Science, 347, 768–771.

Janke N.C. (1966). *Effect of shape upon the settling velocity of regular convex geometric particles*. J. Sedimentary Petrology, 36(2), 370-376.

Julien, P. (1995). Erosion and sedimentation, Cambridge University Press, Cambridge, U.K.

Kaiser, D., Kowalski, N., Waniek, J.J. (2017). Effects of biofouling on the sinking behavior of microplastics. Env. Research Letters, 12(12), 124003.

Kaskas A. (1964). Berechnung der stationären und instationären Bewegung von Kugeln in ruhenden und strömende Medien. Dipl. Thermodynamik und Verfahrenstechnik, TU Berlin.

Khatmullina, L., Isachenko, I. (2017). Settling velocity of microplastic particles of regular shapes. Mar. Pollut. Bull, 114, 871—880.

Kooi, M., Nes, E.H.V., Scheffer, M., Koelmans, A.A. (2017). Ups and downs in the ocean: effects of biofouling on vertical transport of microplastics. Env. Science & Technology, 51(14), 7963-7971.

Kowalski, N., Reichardt, A.M., Waniek, J.J. (2016). Sinking rates of microplastics and potential implications of their alteration by physical, biological, and chemical factors. Mar. Pollut. Bull., 109, 310—319.

Kramer, O.J.I., de Moel, P.J., Raaghav, S.K.R., Baars, E.T., van Vugt, W.H., Breugem, W.-P., Padding, J.T., van der Hoek, J. P. (2021). Can terminal settling velocity and drag of natural particles in water ever be predicted accurately? Drink. Water Eng. Sci., 14, 53–71.

Kreczak, H., Willmott, A.J., Baggaley, A.W. (2021). Subsurface dynamics of buoyant micro-plastics subject to algal biofouling. Limnology and Oceanography, 66(9), 3287-3299.

Krumbein W.C. (1941). Measurement and geological significance of shape and roundness of sedimentary particles. J. Sedimentary Petrology, 11: 64-72.

Laursen, S.N., Fruergaard, M., Andersen, T.J. (2022). Rapid flocculation and settling of positively buoyant microplastic and fine-grained sediment in natural seawater. Marine Pollution Bulletin, 178, 113619.

Leith, D. (1987). Drag on nonspherical objects. Aerosol Sci. Tech., 6, 153-161.

Leiser, R., Schumann, M., Dadi, T., Wendt-Potthoff, K. (2021). Burial of microplastics in fresh-water sediments facilitated by iron-organo flocs. Scientific Reports, 11(1), 1-12.

Li, B., Zhao, J., Ge, W., Li, W., Yuan, H. (2022). Coagulation-flocculation performance and floc properties for microplastics removal by magnesium hydroxide and PAM. J. Env. Chem. Eng., 10(2), 107263.

Li, Y., Wang, X., Fu, W., Xia, X., Liu, C., Min, J., ... Crittenden, J. C. (2019). Interactions between nano/micro plastics and suspended sediment in water: Implications on aggregation and settling. Water Research, 161, 486-495.

Lobelle, D., Kooi, M., Koelmans, A. A., Laufkötter, C., Jongedijk, C. E., Kehl, C., van Sebille, E. (2021). Global modeled sinking characteristics of biofouled microplastic. J. Geophysical Research: Oceans, 126(4), e2020JC017098.

Lusher, A. (2015). Microplastics in the marine environment: distribution, interactions and effects. Marine Anthropogenic Litter, 245-307.

GMR Plastics Europe, Conversion Market & Strategy GmbH. Plastics—The Facts 2019.

Mei, R. (1994). Effect of turbulence on the particle settling velocity in the nonlinear drag range. Int. J. Multiphase Flow, 20(2), 273-284.

Mendrik, F., Fernández, R., Hackney, C.R., Waller, C., Parsons, D.R. (2023). Non-buoyant micro-plastic settling velocity varies with biofilm growth and ambient water salinity. Communications Earth & Environment, 4(1), 30.

Miao, L., Gao, Y., Adyel, T. M., Huo, Z., Liu, Z., Wu, J., Hou, J. (2021). Effects of biofilm colonization on the sinking of microplastics in three freshwater environments. J. Hazardous Materials, 413, 125370.

Potthoff, A., Oelschlägel, K., Schmitt-Jansen, M., Rummel, C.D., Kühnel, D. (2017). From the sea to the laboratory: Characterization of microplastic as prerequisite for the assessment of ecotoxicological impact. Integrated Environmental Assessment and Management, 13(3), 500-504.

Revil-Baudard, T., Akutina, Y., Eiff, O. (2017). Settling velocity in a turbulence column and its effect on the suspension profile. EGU General Assembly Conference Abstracts (p. 2238).

Richardson J.F., Zaki W.N. (1954). Sedimentation and fluidisation: Part I. Trans. Inst. Chem. Eng., 32, 35–53

Rochman CM, Browne MA, Underwood AJ, van Franeker JA, Thompson RC, Amaral-Zettler LA (2016). The ecological impacts of marine debris: unraveling the demonstrated evidence from what is perceived. Ecology 97: 302-312.

Schiller, L., Naumann, A. (1933). Über die grundlegenden Berechnungen bei der Schwerkraft-aufbereitung. Z. Ver. Deutsch. Ing. 77, 318-320.

Shettigar, N.A., Bi, Q., Toorman, E.A. (2024). Assimilating the size diversity: Population Balance Equations applied to the modelling of microplastics transport. Environmental Science & Technology, DOI: 10.1021/acs.est.4c02223.

Soulsby, R. (1997). Dynamics of marine sands, a manual for practical applications, Thomas Telford, London.

*Stokes, G.G. (1851). On the effect of the internal friction on the motion of pendulums. Cambridge Phil. Trans., 9: 8-106.*

Toorman, E.A., Bi, Q., Wongsoredjo, S., Shen, X., Arp, H.P.H, Issler, D. (2017). Modelling microplastics dispersal: anthropogenic cohesive particles and their fate in coastal waters; Poster presented at INTERCOH2017 (13-17 November 2017, Montevideo, Uruguay). DOI: 10.13140/RG.2.2.19975.91041

Toorman, E.A., Brekke Olsen, L.M., Berrojalbiz, N., Issler, D., Oelschlägel, K., Arp, H.P.H. (2018). On the settling behavior of microplastic particles. WEATHER-MIC Project Report, Hydraulics Laboratory, KU Leuven.

Toorman E.A. (2002). Modeling of turbulent flow with cohesive sediment. In: Proc. in Marine Science, Vol.5: Fine Sediment Dynamics in the Marine Environment (J.C. Winterwerp & C. Kranenburg, eds.), pp.155-169, Elsevier Science, Amsterdam.

Toorman. E, (2022) Modification of the Dietrich (1982) formula and a new closure for the terminal settling velocity of spherical particles, Internal note, Hydraulics Laboratory, KU Leuven.

Turton R., Clark N.N. (1987). An explicit relationship to predict spherical particle terminal velocity. Powder Technol, 53, 127-129.

Wadell, H. (1932). Volume, shape, and roundness of rock particles. J. Geology, 40: 443-451.

Waldschläger, K., Schüttrumpf, H. (2019). Effects of particle properties on the settling and rise velocities of microplastics in freshwater under laboratory conditions. Environ. Sci. Technol, 53, 1958-1966.

Williams, G. (1966). Particle roundness and surface texture effects on fall velocity. J. Sediment. Petrol., 36(1), 255–259.

Wu, W., Wang, S.S. (2006). Formulas for sediment porosity and settling velocity. J. Hydr. Eng., 132(8), 858-862.

Zhou, Q., Cheng, N.S. (2009). Experimental investigation of single particle settling in turbulence generated by oscillating grid. Chemical Engineering Journal, 149(1-3), 289-300.